Global water cycle shifts substantially beyond stable pre-industrial conditions

This is a non-peer reviewed preprint submitted to EarthArXiv, which has been submitted to *Science*

Authors: Miina Porkka[1,2]*†, Vili Virkki[1]*†, Lan Wang-Erlandsson[3,4], Dieter Gerten[5,6], Tom Gleeson[7,8], Chinchu Mohan[7,9], Ingo Fetzer[3,4], Fernando Jaramillo[4,10], Arie Staal[11], Sofie te Wierik[12], Arne Tobian[3,5], Ruud van der Ent[13], Petra Döll[14,15], Martina Flörke[16], Simon N. Gosling[17], Naota Hanasaki[18], Yusuke Satoh[19,20], Hannes Müller Schmied[14,15], Niko Wanders[21], Johan Rockström[1,5], Matti Kummu[1]

Affiliations:

[1]Water and Development Research Group, Aalto University; Espoo, Finland.

[2]Global Economic Dynamics and the Biosphere, Royal Swedish Academy of Sciences; Stockholm, Sweden.

[3]Stockholm Resilience Centre, Stockholm University; Stockholm, Sweden.

[4]Bolin Centre for Climate Research, Stockholm University; Stockholm, Sweden.

[5]Potsdam Institute for Climate Impact Research (PIK), Member of the Leibniz Association; Potsdam, Germany.

[6]Geography Department and IRI THESys, Humboldt-Universität zu Berlin; Berlin, Germany.

[7]Department of Civil Engineering, University of Victoria; Victoria, British Columbia, Canada.

[8]School of Earth and Ocean Sciences, University of Victoria; Victoria, British Columbia, Canada.

[9]Global Institute for Water Security, University of Saskatchewan; Saskatoon, Saskatchewan, Canada.

[10]Department of Physical Geography, Stockholm University; Stockholm, Sweden.

[11]Copernicus Institute of Sustainable Development, Utrecht University; Utrecht, Netherlands.

[12]Institute for Biodiversity and Ecosystem Dynamics, Governance and Inclusive Development, University of Amsterdam; Amsterdam, Netherlands.

[13]Department of Water Management, Delft University of Technology; Delft, Netherlands.

[14]Institute of Physical Geography, Goethe University Frankfurt; Frankfurt, Germany.

[15]Senckenberg Leibniz Biodiversity and Climate Research Centre Frankfurt (SBiK-F); Frankfurt, Germany.

[16]Institute of Engineering Hydrology and Water Resources Management, Ruhr-University Bochum; Bochum, Germany.

[17]School of Geography, University of Nottingham; Nottingham, NG7 2RD, United Kingdom.

[18]Center for Climate Change Adaptation, National Institute for Environmental Studies; Tsukuba, Japan.

[19]Moon Soul Graduate School of Future Strategy, Korea Advanced Institute of Science and Technology; Daejeon, Korea.

[20]International Institute for Applied Systems Analysis; Laxenburg, Austria.

[21]Department of Physical Geography, Utrecht University; Utrecht, Netherlands.

*Corresponding author. Email: miina.porkka@aalto.fi, vili.virkki@aalto.fi

†These authors contributed equally to this work.

Abstract: Human actions compromise the many life-supporting functions of the global freshwater cycle. Yet, an encompassing analysis of humanity's aggregate impact on the freshwater cycle is still missing. We compare the current state of the freshwater cycle against a stable reference state by estimating the global area experiencing streamflow and soil moisture deviations beyond pre-industrial variability range. We propose replacing the current *freshwater use* planetary boundary (PB) with our thus-defined *freshwater change* PB. Our analysis indicates unprecedented change: locally, the impacts of e.g. climate change, land use, and dams, are clearly visible. Globally, we find 70% and 44% increases in areas experiencing streamflow and soil moisture deviations. This suggests a transgression of the PB, calling for urgent actions to reduce human disturbance of the freshwater cycle.

One-Sentence Summary: Human disturbance of the global water cycle has led to a trajectory away from stability – locally, regionally, and globally.

Main Text: Freshwater is fundamental to all life on Earth. Various human pressures – such as water and land use, climate change, and water infrastructure – now considerably modify the quantity and timing of freshwater flows, with crucial implications for Earth's climate and ecosystems (*1*). Remarkable signals of water cycle changes include widespread and severe river flow regime alterations (*2*), intensification (*3*) and homogenization (*4*) of the global water cycle, and increases in the severity, frequency, and duration of extreme events (*5*). Despite the alarming evidence of freshwater change, a comprehensive assessment of humanity's aggregate impact on the freshwater cycle and its life-supporting functions is still missing.

The global freshwater cycle's integral role in a resilient Earth system is acknowledged by including freshwater use as one of the nine planetary boundaries (PBs; represented by *control variables*), which set safe boundaries to processes that together regulate the state of the Earth system (*6*, *7*). Initially, the freshwater use PB was defined by annual global *blue water* (surface and groundwater) consumption as a proxy control variable that reflects precipitation partitioning into blue and *green water* (terrestrial evaporation and soil moisture) flows and stocks, and integrates the anthropogenic drivers impacting them (*8*).

The original assessment estimated human modifications of freshwater to be within safe boundaries, but later estimates with more nuanced quantification of water availabilities (*9*) and water consumption – by explicitly including also consumptive use of green water (*10*) – suggested the PB is either being rapidly approached or has already been transgressed. Nevertheless, the most recent update of the PB framework (*7*) concluded that the globally aggregated status of the freshwater use PB is safe, although recognizing transgressions at the basin scale, where safe boundaries were set based on minimum acceptable levels of river flows to maintain an adequate state of aquatic ecosystems.

In addition to the conflicting results of freshwater PB assessments, both the original and more recent PB estimates have been criticized for their limited capacity to capture the interconnected direct and indirect anthropogenic pressures on the water cycle (*11*). These include e.g. land use and land cover change, and anthropogenic greenhouse gas and aerosol emissions, which alter evaporation, soil moisture, precipitation and runoff patterns (*12–16*). Previous approaches have also been criticized for aggregating freshwater fluxes too broadly, e.g. by operating on an annual scale or simply summing global water use and availability despite diverse local impacts (*17*, *18*). These simplifications may conceal important variation across space and time and overlook, or cancel out, the often-contrasting impacts of human drivers on different parts of the water cycle. For example, irrigation decreases streamflow but increases soil moisture, and hydropower operations increase evaporation by reservoir impoundment, as well as shift water flows temporally from the wet to the dry season and blue water scarcity hotspots from upstream to downstream (*19*).

To acknowledge these limitations, recent studies have proposed sub-dividing the freshwater PB into blue and green water components and adopting a bottom-up, area-based approach (*1*, *11*, *20*). Recently, a provisional analysis of Wang-Erlandsson et al. (*20*) proposed that the freshwater PB should describe *change* rather than *use*, and found a likely transgression of the green water component. Yet, previous works have not assessed how the blue and green water components coevolve, or where the geographical hotspots of change are located. We advance the previous work in three major ways: 1) representing the water cycle more comprehensively by including both blue and green water components, 2) presenting the spatial distribution of freshwater change to allow validation against previously reported local and regional freshwater changes and

identification of priority areas for mitigation, and 3) utilizing a wide array of consistently forced global hydrological models to capture inter-model uncertainties (*21*).

Following the recent developments, we propose replacing the original *freshwater use PB* with two control variables for *freshwater change*, which measure the global area with streamflow (blue water) or root-zone soil moisture (hereinafter referred to as soil moisture; green water) deviations beyond variability during the relatively undisturbed pre-industrial period. Widespread deviations from that 'pristine' state can be considered to pose elevated risks to the Earth system functions of freshwater. For example, terrestrial and freshwater ecosystems have adapted to specific quantities and timing of water flows (*22–24*), and wetness of landscapes regulates climate from micro- to regional and global scales, such that changes in (timing of) wetness in one location can impact rainfall and consequently streamflow and soil moisture both locally and remotely (*25*).

We used streamflow and soil moisture data simulated by an ensemble of state-of-the-art gridded global hydrological models forced with consistent and bias-adjusted CMIP5 climate models and dynamic socio-economic conditions (Table S1) (*21*). Based on a 200-year pre-industrial reference period, we determined the range of normal variability (defined as 5^{th}–95^{th} percentile values) for each 0.5° grid cell and month, and compared historical (1861–2005) values against these bounds to detect local deviations that are either dry (value below the 5^{th} percentile) or wet (value above the 95^{th} percentile) (Fig. S1). We aggregated the local deviations – at regional and global scales – to *the percentage of ice-free land area with streamflow or soil moisture deviations from pre-industrial variability*. These constitute the two control variables (blue and green water) that represent cumulative impacts on the water cycle – globally and regionally.

We found streamflow and soil moisture conditions to be stable during the pre-industrial period. No visible trends in the percentage of global area with freshwater deviations were observed, and apart from a few outliers, it varied within +/- 1.5 percentage points (pp) of the pre-industrial median (9.3% of global area for blue water, 9.8% for green water). Pending robust quantifications of Earth system-wide responses to water cycle modifications surpassing the pre-industrial variability range, we propose the 95^{th} percentile of pre-industrial global area with deviations (i.e. occurring expectedly once in 20 years) as the new PB for freshwater change. This corresponds to 10.4% of global area for blue water and 11.0% for green water (Fig. 1). We hypothesize that persistent exceedance beyond these boundaries represents an unprecedented shift in the global water cycle, and an elevated risk of weakening freshwater-dependent life-supporting functions.

The global area with streamflow and soil moisture deviations started to steadily increase soon after the pre-industrial period (Fig. 1). The 10-year moving mean of global area with streamflow deviations permanently transgressed the PB (10.4%) in 1912 (ensemble 25^{th} percentile in 1970), and the degree of transgression continued to increase apart from two dips around 1940 and 1970. Areas with wet or dry streamflow deviations currently (mean of 1996–2005) cover 17.7% (~ 23 million km^2) of global area (Fig. 1a). This corresponds to a 70% (7.3 pp) increase compared to the PB and 90% (8.4 pp) compared to the median of the pre-industrial variability range. Considering the narrow (~ 3 pp) pre-industrial variability range, these changes are substantial. A closer inspection indicates that dry streamflow deviations were still increasing in spatial coverage by the end of our study period, while wet deviations had plateaued (Fig. S6b, c).

Green water change exhibits a similar, though slightly less severe pattern: the PB (11.0% of global area) was permanently transgressed in 1928 (ensemble 25^{th} percentile in 1975), after

which the area with soil moisture deviations has consistently increased, apart from the two dips in the latter half of the 20th century (Fig. 1b), which were also visible for blue water. During the last decade of our analysis period, soil moisture deviations occurred on 15.8% (~ 20 million km^2) of global land, which is 43% (4.8 pp) above the PB and 61% (6.0 pp) above the pre-industrial median. Opposite to streamflow deviations, wet soil moisture deviations continued to increase towards the end of the 20th century, while dry deviations were even declining slowly, yet remaining considerably higher than during the pre-industrial period (Fig. S6e, f).

Our regional (river basin) aggregation of deviations shows that some regions transgressed their upper limit of pre-industrial variability range (95th percentile) only in the late 20th century or not yet at all (Fig. S7). Furthermore, mapping grid-level changes in the frequency of streamflow and soil moisture deviations (Fig. 2, S8) reveals a general pattern of more frequent dry deviations of both streamflow and soil moisture in much of the tropics and subtropics, with wet deviations becoming more common in temperate and subpolar regions, and in many highland areas. This global pattern likely arises from the precipitation change due to 1°C of mean global warming (*5*), which affects both streamflow and soil moisture similarly if major human impacts on land surface, such as land cover change and soil degradation, do not change precipitation partitioning into blue and green water.

In contrast, increased frequency of dry streamflow deviations in combination with wet soil moisture deviations in a given area most likely indicates an effect of irrigation expansion. Indeed, we observe these cases in many heavily irrigated regions (*26*), such as South Asia, eastern China, Western USA and the Nile delta (Fig. 3, pink color). These regions are also the likely early drivers of globally aggregated deviations, as their irrigation extent was relatively large already at the beginning of the 20th century (*26*). The Mississippi, Indus, and Nile basins, for instance, were among the first regions where the extent of streamflow deviations permanently transgressed their upper limit of pre-industrial variability range – in the Nile, this occurred also for soil moisture deviations (Fig. S7).

Increases in both wet and dry streamflow deviations, as well as wet soil moisture deviations, indicates another type of direct anthropogenic change (Fig. 3, dark blue). This could imply a situation in which the natural river flow regime has been altered by dam operation (decreased flood peaks and increased dry season streamflow) in combination with extensive irrigation (decreased streamflow, increased soil moisture). These cases can be found in many heavily modified river basins, such as the Nile, the Aral Sea , and parts of India and Thailand (Fig. 3) (*27*).

The very distinct changes in the Sahel suggest effects of a more variable climate. Dry conditions (relative to pre-industrial climate) dominated in the region already in the first half of the 20th century (Fig. S9) and intensified from the 1970s onwards (Fig. 2) (*28*). Recent decades have additionally witnessed widespread wet deviations (and different combinations of dry and wet), which could be explained by changes in temporal dynamics, such as intensity of precipitation, number of wet days, occurrence of dry spells and timing and length of the rainy season (*28*, *29*).

The observed changes are consistent with many regional to global freshwater-mediated impacts that have been reported. One of the most dramatic examples of blue water change is the Aral Sea, where overuse of water for irrigation resulted in lake depletion, consequent ecological degradation, and regional climate change (*30*). This development is clearly visible in our data, which shows a steep increase in dry streamflow and a moderate increase in wet soil moisture

deviations in the Amu Darya (Fig. 3) and Syr Darya basins starting in the late 1960s – in accordance with the substantial irrigation expansion that started in the region at that time (*30*).

Green water changes have been associated with productivity loss, as exemplified by drying-induced forest dieback in many of the regions where we observed a major increase in dry soil moisture deviations, such as the Mediterranean basin, central North America and West Africa (e.g. Niger river basin in Fig. 3) (*31*). Productivity shocks due to dry and wet soil moisture deviations (droughts and floods) have been reported also in cultivated lands, particularly in South and East Asia, Australia and North Africa (*32*), where we find both drying and wetting (Fig. 2b, India in Fig. 3). Other examples of ecological and climatic impacts of water surpluses are habitat loss in the Central Amazon floodplains due to anthropogenic flood pulse disturbance (*33*), and increased greenhouse gas emissions from reservoirs (*34*), both created by dam construction and operation, though these freshwater alterations are relatively small-scale and thus not clearly visible in our maps.

The profound human-driven water cycle changes shown here may already compromise freshwater's role for a resilient Earth system. However, uncertainties remain related not only to our computational method but also to the exact position of the PB along the proposed control variables of freshwater change (Supplementary Text). Earth system-wide responses of water cycle modifications are too complex to be quantified with our current knowledge, and it is possible that the level of freshwater modifications that triggers rapid state changes in the Earth system can only be determined in retrospect. Although it is likely that buffers in the Earth system allow for greater variability in the water cycle compared to the pre-industrial period, the precautionary principle of the PB framework (*8*) motivates a conservative placement of the new PB for freshwater change at the lower level of scientific uncertainty. We consider this to be at the upper end (95th percentile) of pre-industrial variability range, which can be regarded as highly precautionary – although an even stricter boundary placement could also be justified, due to signs of weakened Earth system resilience (*20*) and the complex interactions between freshwater and other PBs (*35*).

Regardless of the exact position of the freshwater change PB, however, we have shown that the rate and extent of freshwater change has been unprecedented after the pre-industrial period: globally, areas with streamflow and soil moisture deviations have increased by 70–90 and 44–61%, respectively. Locally, evidence of freshwater-triggered ecological and climatic shifts has been mounting as the main components of the freshwater cycle have moved further outside of the pre-industrial variability range. Our findings indicate a likely transgression of the new PB for freshwater change already around the mid-20th century, while climate change (*36*), deforestation (*37*) and many other human pressures on the water cycle continue to pose a major risk of further change. This calls for urgent action to reduce human disturbance of the water cycle.

References

1. T. Gleeson, L. Wang-Erlandsson, M. Porkka, S. C. Zipper, F. Jaramillo, D. Gerten, I. Fetzer, S. E. Cornell, L. Piemontese, L. J. Gordon, J. Rockström, T. Oki, M. Sivapalan, Y. Wada, K. A. Brauman, M. Flörke, M. F. P. Bierkens, B. Lehner, P. Keys, M. Kummu, T. Wagener, S. Dadson, T. J. Troy, W. Steffen, M. Falkenmark, J. S. Famiglietti, Illuminating water cycle modifications and Earth system resilience in the Anthropocene. *Water Resour Res*. **56**, e2019WR02495 (2020).

2. V. Virkki, E. Alanärä, M. Porkka, L. Ahopelto, T. Gleeson, C. Mohan, L. Wang-Erlandsson, M. Flörke, D. Gerten, S. N. Gosling, N. Hanasaki, H. Müller Schmied, N. Wanders, M. Kummu, Globally widespread and increasing violations of environmental flow envelopes. *Hydrol. Earth Syst. Sci*. **26**, 3315–3336 (2022).

3. T. G. Huntington, Evidence for intensification of the global water cycle: Review and synthesis. *J. Hydrol*. **319**, 83–95 (2006).

4. D. F. Levia, I. F. Creed, D. M. Hannah, K. Nanko, E. W. Boyer, D. E. Carlyle-Moses, N. van de Giesen, D. Grasso, A. J. Guswa, J. E. Hudson, S. A. Hudson, S. Iida, R. B. Jackson, G. G. Katul, T. Kumagai, P. Llorens, F. L. Ribeiro, D. E. Pataki, C. A. Peters, D. S. Carretero, J. S. Selker, D. Tetzlaff, M. Zalewski, M. Bruen, Homogenization of the terrestrial water cycle. *Nat. Geosci.* **13**, 656–658 (2020).

5. H. K. Douville, K. Raghavan, J. Renwick, R. P. Allan, P. A. Arias, M. Barlow, R. Cerezo-Mota, A. Cherchi, T. Y. Gan, J. Gergis, D. Jiang, A. Khan, W. Pokam Mba, D. Rosenfeld, J. Tierney, and O. Zolina, "Water Cycle Changes" in *Climate Change 2021: The Physical Science Basis. Contribution of Working Group I to the Sixth Assessment Report of the Intergovernmental Panel on Climate Change*, V. P. Masson-Delmotte, V., P. Zhai, A. Pirani, S.L. Connors, C. Péan, S. Berger, N. Caud, Y. Chen, L. Goldfarb, M.I. Gomis, M. Huang, K. Leitzell, E. Lonnoy, J.B.R. Matthews, T.K. Maycock, T. Waterfield, O. Yelekçi, R. Yu, and B. Zhou, Eds. (Cambridge University Press, 2021).

6. J. Rockström, W. Steffen, K. Noone, Å. Persson, F. S. Chapin, E. F. Lambin, T. M. Lenton, M. Scheffer, C. Folke, H. J. Schellnhuber, B. Nykvist, C. A. de Wit, T. Hughes, S. van der Leeuw, H. Rodhe, S. Sörlin, P. K. Snyder, R. Costanza, U. Svedin, M. Falkenmark, L. Karlberg, R. W. Corell, V. J. Fabry, J. Hansen, B. Walker, D. Liverman, K. Richardson, P. Crutzen, J. A. Foley, A safe operating space for humanity. *Nature*. **461**, 472–475 (2009).

7. W. Steffen, K. Richardson, J. Rockström, S. E. Cornell, I. Fetzer, E. M. Bennett, R. Biggs, S. R. Carpenter, W. de Vries, C. A. de Wit, C. Folke, D. Gerten, J. Heinke, G. M. Mace, L. M. Persson, V. Ramanathan, B. Reyers, S. Sörlin, Planetary boundaries: Guiding human development on a changing planet. *Science*. **347**, 1259855 (2015).

8. J. Rockström, W. Steffen, K. Noone, Å. Persson, F. S. I. Chapin, E. Lambin, T. Lenton, M. Scheffer, C. Folke, H. J. Schellnhuber, B. Nykvist, C. de Wit, T. Hughes, S. van der Leeuw, H. Rodhe, S. Sörlin, P. Snyder, R. Costanza, U. Svedin, M. Falkenmark, L. Karlberg, R. Corell, V. Fabry, J. Hansen, B. Walker, D. Liverman, K. Richardson, P. Crutzen, J. Foley, Planetary Boundaries: Exploring the Safe Operating Space for Humanity. *Ecol. Soc.* **14**, 32 (2009).

9. D. Gerten, H. Hoff, J. Rockström, J. Jägermeyr, M. Kummu, A. V. Pastor, Towards a revised planetary boundary for consumptive freshwater use: role of environmental flow requirements. *Curr Opin Environ Sustain*. **5**, 551–558 (2013).

10. F. Jaramillo, G. Destouni, Local flow regulation and irrigation raise global human water consumption and footprint. *Science*. **350**, 1248–1251 (2015).

11. T. Gleeson, L. Wang-Erlandsson, S. C. Zipper, M. Porkka, F. Jaramillo, D. Gerten, I. Fetzer, S. E. Cornell, L. Piemontese, L. J. Gordon, J. Rockström, T. Oki, M. Sivapalan, Y. Wada, K. A. Brauman, M. Flörke, M. F. P. Bierkens, B. Lehner, P. Keys, M. Kummu, T. Wagener, S. Dadson, T. J. Troy, W. Steffen, M. Falkenmark, J. S. Famiglietti, The Water Planetary Boundary: Interrogation and Revision. *One Earth*. **2**, 223–234 (2020).

12. D. Lawrence, K. Vandecar, Effects of tropical deforestation on climate and agriculture. *Nature Clim Change*. **5**, 27–36 (2015).

13. J. Liu, B. Wang, M. A. Cane, S.-Y. Yim, J.-Y. Lee, Divergent global precipitation changes induced by natural versus anthropogenic forcing. *Nature*. **493**, 656–659 (2013).

14. M. J. Puma, B. I. Cook, Effects of irrigation on global climate during the 20th century. *J. Geophys. Res. Atmos*. **115**, D16120 (2010).

15. J. Sillmann, C. W. Stjern, G. Myhre, B. H. Samset, Ø. Hodnebrog, T. Andrews, O. Boucher, G. Faluvegi, P. Forster, M. R. Kasoar, V. V. Kharin, A. Kirkevåg, J.-F. Lamarque, D. J. L. Olivié, T. B. Richardson, D. Shindell, T. Takemura, A. Voulgarakis, F. W. Zwiers, Extreme wet and dry conditions affected differently by greenhouse gases and aerosols. *npj Clim Atmos Sci*. **2**, 24 (2019).

16. S. M. Sterling, A. Ducharne, J. Polcher, The impact of global land-cover change on the terrestrial water cycle. *Nature Clim Change*. **3**, 385–390 (2013).

17. M. Heistermann, HESS Opinions: A planetary boundary on freshwater use is misleading. *Hydrol. Earth Syst. Sci*. **21**, 3455–3461 (2017).

18. J. Bunsen, M. Berger, M. Finkbeiner, Planetary boundaries for water – A review. *Ecol. Indic*. **121**, 107022 (2021).

19. T. I. E. Veldkamp, Y. Wada, J. C. J. H. Aerts, P. Döll, S. N. Gosling, J. Liu, Y. Masaki, T. Oki, S. Ostberg, Y. Pokhrel, Y. Satoh, H. Kim, P. J. Ward, Water scarcity hotspots travel downstream due to human interventions in the 20th and 21st century. *Nat Commun*. **8**, 15697 (2017).

20. L. Wang-Erlandsson, A. Tobian, R. J. van der Ent, I. Fetzer, S. te Wierik, M. Porkka, A. Staal, F. Jaramillo, H. Dahlmann, C. Singh, P. Greve, D. Gerten, P. W. Keys, T. Gleeson, S. E. Cornell, W. Steffen, X. Bai, J. Rockström, A planetary boundary for green water. *Nat Rev Earth Environ*. **3**, 380–392 (2022).

21. Materials and methods are available as supplementary materials.

22. M. Berdugo, M. Delgado-Baquerizo, S. Soliveres, R. Hernández-Clemente, Y. Zhao, J. J. Gaitán, N. Gross, H. Saiz, V. Maire, A. Lehmann, M. C. Rillig, R. V. Solé, F. T. Maestre, Global ecosystem thresholds driven by aridity. *Science*. **367**, 787–790 (2020).

23. P. Meir, T. E. Wood, D. R. Galbraith, P. M. Brando, A. C. L. Da Costa, L. Rowland, L. V. Ferreira, Threshold Responses to Soil Moisture Deficit by Trees and Soil in Tropical Rain Forests: Insights from Field Experiments. *BioScience*. **65**, 882–892 (2015).

24. B. Richter, J. Baumgartner, R. Wigington, D. Braun, How much water does a river need? *Freshw. Biol.* **37**, 231–249 (1997).

25. L. Wang-Erlandsson, I. Fetzer, P. W. Keys, R. J. van der Ent, H. H. G. Savenije, L. J. Gordon, Remote land use impacts on river flows through atmospheric teleconnections. *Hydrol. Earth Syst. Sci*. **22**, 4311–4328 (2018).

26. S. Siebert, M. Kummu, M. Porkka, P. Döll, N. Ramankutty, B. R. Scanlon, A global data set of the extent of irrigated land from 1900 to 2005. *Hydrol. Earth Syst. Sci*. **19**, 1521–1545 (2015).

27. B. Lehner, C. R. Liermann, C. Revenga, C. Vörösmarty, B. Fekete, P. Crouzet, P. Döll, M. Endejan, K. Frenken, J. Magome, C. Nilsson, J. C. Robertson, R. Rödel, N. Sindorf, D. Wisser, High-resolution mapping of the world's reservoirs and dams for sustainable river-flow management. *Front Ecol Environ*. **9**, 494–502 (2011).

28. M. Biasutti, Rainfall trends in the African Sahel: Characteristics, processes, and causes. *Wiley Interdiscip Rev Clim Change*. **10**, e591 (2019).

29. M. Porkka, L. Wang-Erlandsson, G. Destouni, A. M. L. Ekman, J. Rockström, L. J. Gordon, Is wetter better? Exploring agriculturally-relevant rainfall characteristics over four decades in the Sahel. *Environ. Res. Lett.* **16**, 035002 (2021).

30. P. Micklin, The Aral Sea disaster. *Annu. Rev. Earth Planet. Sci*. **35**, 47–7272 (2007).

31. W. M. Hammond, A. P. Williams, J. T. Abatzoglou, H. D. Adams, T. Klein, R. López, C. Sáenz-Romero, H. Hartmann, D. D. Breshears, C. D. Allen, Global field observations of tree die-off reveal hotter-drought fingerprint for Earth's forests. *Nat Commun*. **13**, 1761 (2022).

32. R. S. Cottrell, K. L. Nash, B. S. Halpern, T. A. Remenyi, S. P. Corney, A. Fleming, E. A. Fulton, S. Hornborg, A. Johne, R. A. Watson, J. L. Blanchard, Food production shocks across land and sea. *Nat Sustain*. **2**, 130–137 (2019).

33. J. Schöngart, F. Wittmann, A. Faria de Resende, C. Assahira, G. de Sousa Lobo, J. Rocha Duarte Neves, M. da Rocha, G. Biem Mori, A. Costa Quaresma, L. Oreste Demarchi, B. Weiss Albuquerque, Y. Oliveira Feitosa, G. da Silva Costa, G. Vieira Feitoza, F. Machado Durgante, A. Lopes, S. E. Trumbore, T. Sanna Freire Silva, H. ter Steege, A. L. Val, W. J. Junk, M. T. F. Piedade, The shadow of the Balbina dam: A synthesis of over 35 years of downstream impacts on floodplain forests in Central Amazonia. *Aquat Conserv*. **31**, 1117–1135 (2021).

34. B. R. Deemer, J. A. Harrison, S. Li, J. J. Beaulieu, T. DelSontro, N. Barros, J. F. Bezerra-Neto, S. M. Powers, M. A. dos Santos, J. A. Vonk, Greenhouse Gas Emissions from Reservoir Water Surfaces: A New Global Synthesis. *BioScience*. **66**, 949–964 (2016).

35. A. Chrysafi, V. Virkki, M. Jalava, V. Sandström, J. Piipponen, M. Porkka, S. Lade, K. L. Mere, L. Wang-Erlandsson, L. Scherer, L. Andersen, E. Bennett, K. Brauman, G. Cooper, A. D. Palma, P. Döll, A. Downing, T. DuBois, I. Fetzer, E. Fulton, D. Gerten, H. Jaafar, J. Jaegermeyr, F. Jaramillo, M. Jung, H. Kahiluoto, A. Mackay, L. Lassaletta, D. Mason-D'Croz, M. Mekonnen, K. Nash, A. Pastor, N. Ramankutty, B. Ridoutt, S. Siebert, B. Simmons, A. Staal, Z. Sun, A. Tobian, A. Usubiaga-Liaño, R. van der Ent, A. van Soesbergen, P. Verburg, Y. Wada, S. Zipper, M. Kummu, Quantifying Earth system interactions for sustainable food production via expert elicitation (in press), *Nat Sustain*.

36. S. Stevenson, S. Coats, D. Touma, J. Cole, F. Lehner, J. Fasullo, B. Otto-Bliesner, Twenty-first century hydroclimate: A continually changing baseline, with more frequent extremes. *PNAS*. **119**, e2108124119 (2022).

37. C. A. Boulton, T. M. Lenton, N. Boers, Pronounced loss of Amazon rainforest resilience since the early 2000s. *Nat. Clim. Chang.* **12**, 271–278 (2022).

38. R Core Team, *R: A language and environment for statistical computing.* (R Foundation for Statistical Computing, Vienna, Austria, 2022; https://www.R-project.org).

39. K. Frieler, S. Lange, F. Piontek, C. P. O. Reyer, J. Schewe, L. Warszawski, F. Zhao, L. Chini, S. Denvil, K. Emanuel, T. Geiger, K. Halladay, G. Hurtt, M. Mengel, D. Murakami, S. Ostberg, A. Popp, R. Riva, M. Stevanovic, T. Suzuki, J. Volkholz, E. Burke, P. Ciais, K. Ebi, T. D. Eddy, J. Elliott, E. Galbraith, S. N. Gosling, F. Hattermann, T. Hickler, J. Hinkel, C. Hof, V. Huber, J. Jägermeyr, V. Krysanova, R. Marcé, H. Müller Schmied, I. Mouratiadou, D. Pierson, D. P. Tittensor, R. Vautard, M. van Vliet, M. F. Biber, R. A. Betts, B. L. Bodirsky, D. Deryng, S. Frolking, C. D. Jones, H. K. Lotze, H. Lotze-Campen, R. Sahajpal, K. Thonicke, H. Tian, Y. Yamagata, Assessing the impacts of 1.5 °C global warming – simulation protocol of the Inter-Sectoral Impact Model Intercomparison Project (ISIMIP2b). *Geosci. Model Dev*. **10**, 4321–4345 (2017).

40. L. Gudmundsson, J. Boulange, H. X. Do, S. N. Gosling, M. G. Grillakis, A. G. Koutroulis, M. Leonard, J. Liu, H. M. Schmied, L. Papadimitriou, Y. Pokhrel, S. I. Seneviratne, Y. Satoh, W. Thiery, S. Westra, X. Zhang, F. Zhao, Globally observed trends in mean and extreme river flow attributed to climate change. *Science*. **371**, 1159–1162 (2021).

41. S. J. Birkinshaw, P. Moore, C. g. Kilsby, G. M. O'Donnell, A. j. Hardy, P. a. M. Berry, Daily discharge estimation at ungauged river sites using remote sensing. *Hydrol. Process*. **28**, 1043–1054 (2014).

42. J. Peng, A. Loew, O. Merlin, N. E. C. Verhoest, A review of spatial downscaling of satellite remotely sensed soil moisture. *Rev. Geophys*. **55**, 341–366 (2017).

43. A. Dallmeyer, M. Claussen, S. J. Lorenz, T. Shanahan, The end of the African humid period as seen by a transient comprehensive Earth system model simulation of the last 8000 years. *Clim. Past*. **16**, 117–140 (2020).

44. A. Dallmeyer, M. Claussen, S. J. Lorenz, M. Sigl, M. Toohey, U. Herzschuh, Holocene vegetation transitions and their climatic drivers in MPI-ESM1.2. *Clim. Past.* **17**, 2481–2513 (2021).

45. E. C. Ellis, N. Gauthier, K. K. Goldewijk, R. B. Bird, N. Boivin, S. Díaz, D. Q. Fuller, J. L. Gill, J. O. Kaplan, N. Kingston, H. Locke, C. N. H. McMichael, D. Ranco, T. C. Rick, M. R. Shaw, L. Stephens, J.-C. Svenning, J. E. M. Watson, People have shaped most of terrestrial nature for at least 12,000 years. *PNAS*. **118**, e2023483118 (2021).

46. K. E. Taylor, R. J. Stouffer, G. A. Meehl, An Overview of CMIP5 and the Experiment Design. *Bull. Am. Meteorol. Soc*. **93**, 485–498 (2012).

47. D. M. Lawrence, R. A. Fisher, C. D. Koven, K. W. Oleson, S. C. Swenson, G. Bonan, N. Collier, B. Ghimire, L. van Kampenhout, D. Kennedy, E. Kluzek, P. J. Lawrence, F. Li, H. Li, D. Lombardozzi, W. J. Riley, W. J. Sacks, M. Shi, M. Vertenstein, W. R. Wieder, C. Xu, A. A. Ali, A. M. Badger, G. Bisht, M. van den Broeke, M. A. Brunke, S. P. Burns, J. Buzan, M. Clark, A. Craig, K. Dahlin, B. Drewniak, J. B. Fisher, M. Flanner, A. M. Fox, P. Gentine, F. Hoffman, G. Keppel-Aleks, R. Knox, S. Kumar, J. Lenaerts, L. R. Leung, W. H. Lipscomb, Y. Lu, A. Pandey, J. D. Pelletier, J. Perket, J. T. Randerson, D. M. Ricciuto, B. M. Sanderson, A. Slater, Z. M. Subin, J. Tang, R. Q. Thomas, M. Val Martin, X. Zeng, The Community Land Model Version 5: Description of New Features, Benchmarking, and Impact of Forcing Uncertainty. *J. Adv. Model. Earth Syst.* **11**, 4245–4287 (2019).

48. S. Schaphoff, W. von Bloh, A. Rammig, K. Thonicke, H. Biemans, M. Forkel, D. Gerten, J. Heinke, J. Jägermeyr, J. Knauer, F. Langerwisch, W. Lucht, C. Müller, S. Rolinski, K. Waha, LPJmL4 – a dynamic global vegetation model with managed land – Part 1: Model description. *Geosci. Model Dev*. **11**, 1343–1375 (2018).

49. T. Stacke, S. Hagemann, Development and evaluation of a global dynamical wetlands extent scheme. *Hydrol. Earth Syst. Sci*. **16**, 2915–2933 (2012).

50. E. H. Sutanudjaja, R. van Beek, N. Wanders, Y. Wada, J. H. C. Bosmans, N. Drost, R. J. van der Ent, I. E. M. de Graaf, J. M. Hoch, K. de Jong, D. Karssenberg, P. López López, S. Peßenteiner, O. Schmitz, M. W. Straatsma, E. Vannametee, D. Wisser, M. F. P. Bierkens, PCR-GLOBWB 2: a 5 arcmin global hydrological and water resources model. *Geosci. Model Dev*. **11**, 2429–2453 (2018).

51. N. Hanasaki, S. Kanae, T. Oki, K. Masuda, K. Motoya, N. Shirakawa, Y. Shen, K. Tanaka, An integrated model for the assessment of global water resources – Part 1: Model description and input meteorological forcing. *Hydrol. Earth Syst. Sci*. **12**, 1007–1025 (2008).

52. K. Takata, S. Emori, T. Watanabe, Development of the minimal advanced treatments of surface interaction and runoff. *Glob Planet Change*. **38**, 209–222 (2003).

53. H. Müller Schmied, L. Adam, S. Eisner, G. Fink, M. Flörke, H. Kim, T. Oki, F. T. Portmann, R. Reinecke, C. Riedel, Q. Song, J. Zhang, P. Döll, Variations of global and continental water balance components as impacted by climate forcing uncertainty and human water use. *Hydrol. Earth Syst. Sci*. **20**, 2877–2898 (2016).

54. J. P. Dunne, J. G. John, A. J. Adcroft, S. M. Griffies, R. W. Hallberg, E. Shevliakova, R. J. Stouffer, W. Cooke, K. A. Dunne, M. J. Harrison, J. P. Krasting, S. L. Malyshev, P. C. D. Milly, P. J. Phillipps, L. T. Sentman, B. L. Samuels, M. J. Spelman, M. Winton, A. T. Wittenberg, N. Zadeh, GFDL's ESM2 Global Coupled Climate–Carbon Earth System Models. Part I: Physical Formulation and Baseline Simulation Characteristics. *J. Clim*. **25**, 6646–6665 (2012).

55. W. J. Collins, N. Bellouin, M. Doutriaux-Boucher, N. Gedney, P. Halloran, T. Hinton, J. Hughes, C. D. Jones, M. Joshi, S. Liddicoat, G. Martin, F. O'Connor, J. Rae, C. Senior, S. Sitch, I. Totterdell, A. Wiltshire, S. Woodward, Development and evaluation of an Earth-System model – HadGEM2. *Geosci. Model Dev*. **4**, 1051–1075 (2011).

56. J.-L. Dufresne, M.-A. Foujols, S. Denvil, A. Caubel, O. Marti, O. Aumont, Y. Balkanski, S. Bekki, H. Bellenger, R. Benshila, S. Bony, L. Bopp, P. Braconnot, P. Brockmann, P. Cadule, F. Cheruy, F. Codron, A. Cozic, D. Cugnet, N. de Noblet, J.-P. Duvel, C. Ethé, L. Fairhead, T. Fichefet, S. Flavoni, P. Friedlingstein, J.-Y. Grandpeix, L. Guez, E. Guilyardi, D. Hauglustaine, F. Hourdin, A. Idelkadi, J. Ghattas, S. Joussaume, M. Kageyama, G. Krinner, S. Labetoulle, A. Lahellec, M.-P. Lefebvre, F. Lefevre, C. Levy, Z. X. Li, J. Lloyd, F. Lott, G. Madec, M. Mancip, M. Marchand, S. Masson, Y. Meurdesoif, J. Mignot, I. Musat, S. Parouty, J. Polcher, C. Rio, M. Schulz, D. Swingedouw, S. Szopa, C. Talandier, P. Terray, N. Viovy, N. Vuichard, Climate change projections using the IPSL-CM5 Earth System Model: from CMIP3 to CMIP5. *Clim Dyn*. **40**, 2123–2165 (2013).

57. M. Watanabe, T. Suzuki, R. O'ishi, Y. Komuro, S. Watanabe, S. Emori, T. Takemura, M. Chikira, T. Ogura, M. Sekiguchi, K. Takata, D. Yamazaki, T. Yokohata, T. Nozawa, H. Hasumi, H. Tatebe, M. Kimoto, Improved Climate Simulation by MIROC5: Mean States, Variability, and Climate Sensitivity. *J. Clim*. **23**, 6312–6335 (2010).

58. S. Huang, R. Kumar, M. Flörke, T. Yang, Y. Hundecha, P. Kraft, C. Gao, A. Gelfan, S. Liersch, A. Lobanova, M. Strauch, F. van Ogtrop, J. Reinhardt, U. Haberlandt, V. Krysanova, Evaluation of an ensemble of regional hydrological models in 12 large-scale river basins worldwide. *Clim. Change*. **141**, 381–397 (2017).

59. T. I. E. Veldkamp, F. Zhao, P. J. Ward, H. de Moel, J. C. J. H. Aerts, H. M. Schmied, F. T. Portmann, Y. Masaki, Y. Pokhrel, X. Liu, Y. Satoh, D. Gerten, S. N. Gosling, J. Zaherpour, Y. Wada, Human impact parameterizations in global hydrological models improve estimates of monthly discharges and hydrological extremes: a multi-model validation study. *Environ. Res. Lett.* **13**, 055008 (2018).

60. J. Zaherpour, S. N. Gosling, N. Mount, H. M. Schmied, T. I. E. Veldkamp, R. Dankers, S. Eisner, D. Gerten, L. Gudmundsson, I. Haddeland, N. Hanasaki, H. Kim, G. Leng, J. Liu, Y. Masaki, T. Oki, Y. Pokhrel, Y. Satoh, J. Schewe, Y. Wada, Worldwide evaluation of mean and extreme runoff from six global-scale hydrological models that account for human impacts. *Environ. Res. Lett.* **13**, 065015 (2018).

61. J. Zaherpour, N. Mount, S. N. Gosling, R. Dankers, S. Eisner, D. Gerten, X. Liu, Y. Masaki, H. Müller Schmied, Q. Tang, Y. Wada, Exploring the value of machine learning

for weighted multi-model combination of an ensemble of global hydrological models. *Environ Model Softw*. **114**, 112–128 (2019).

62. C.-E. Telteu, H. Müller Schmied, W. Thiery, G. Leng, P. Burek, X. Liu, J. E. S. Boulange, L. S. Andersen, M. Grillakis, S. N. Gosling, Y. Satoh, O. Rakovec, T. Stacke, J. Chang, N. Wanders, H. L. Shah, T. Trautmann, G. Mao, N. Hanasaki, A. Koutroulis, Y. Pokhrel, L. Samaniego, Y. Wada, V. Mishra, J. Liu, P. Döll, F. Zhao, A. Gädeke, S. S. Rabin, F. Herz, Understanding each other's models: an introduction and a standard representation of 16 global water models to support intercomparison, improvement, and communication. *Geosci. Model Dev*. **14**, 3843–3878 (2021).

63. J. Chen, A. K. Gupta, *Parametric statistical change point analysis: With applications to genetics, medicine, and finance* (Birkhäuser Boston, Massachusetts, 2014).

64. R. Killick, I. A. Eckley, changepoint: An R Package for Changepoint Analysis. *J. Stat. Softw*. **58**, 1–19 (2014).

65. J. Chambers, T. Hastie, D. Pregibon, "Statistical Models in S" in: *Compstat, 1st edn*. K. Momirović, V. Mildner, Eds. (Physica-Verlag, 1990).

66. J. Boé, L. Terray, F. Habets, E. Martin, Statistical and dynamical downscaling of the Seine basin climate for hydro-meteorological studies. *Int J Climatol*. **27**, 1643–1655 (2007).

67. L. Gudmundsson, L. M. Tallaksen, K. Stahl, D. B. Clark, E. Dumont, S. Hagemann, N. Bertrand, D. Gerten, J. Heinke, N. Hanasaki, F. Voss, S. Koirala, Comparing Large-Scale Hydrological Model Simulations to Observed Runoff Percentiles in Europe. *J. Hydrometeor.* **13**, 604–620 (2012).

68. K. Klein Goldewijk, A. Beusen, J. Doelman, E. Stehfest, Anthropogenic land use estimates for the Holocene – HYDE 3.2. *Earth Syst. Sci. Data*. **9**, 927–953 (2017).

69. Food and Agriculture Organization of the United Nations (FAO), FAOSTAT Statistical Database. Extracted from: http://www.fao.org/faostat/en. Date of Access: 01-07-2022 (2022).

70. Y. Wada, M. F. P. Bierkens, Sustainability of global water use: past reconstruction and future projections. *Environ. Res. Lett.* **9**, 104003 (2014).

71. C. Zarfl, A. E. Lumsdon, J. Berlekamp, L. Tydecks, K. Tockner, A global boom in hydropower dam construction. *Aquat Sci*. **77**, 161–170 (2015).

72. R. J. Keenan, G. A. Reams, F. Achard, J. V. de Freitas, A. Grainger, E. Lindquist, Dynamics of global forest area: Results from the FAO Global Forest Resources Assessment 2015. *For. Ecol. Manag.*. **352**, 9–20 (2015).

73. A. Gädeke, V. Krysanova, A. Aryal, J. Chang, M. Grillakis, N. Hanasaki, A. Koutroulis, Y. Pokhrel, Y. Satoh, S. Schaphoff, H. Müller Schmied, T. Stacke, Q. Tang, Y. Wada, K. Thonicke, Performance evaluation of global hydrological models in six large Pan-Arctic watersheds. *Clim. Change*. **163**, 1329–1351 (2020).

74. D. Kriebel, J. Tickner, P. Epstein, J. Lemons, R. Levins, E. L. Loechler, M. Quinn, R. Rudel, T. Schettler, M. Stoto, The precautionary principle in environmental science. *Environ Health Perspect*. **109**, 871–876 (2001).

75. B. Lehner, G. Grill, Global river hydrography and network routing: baseline data and new approaches to study the world's large river systems. *Hydrol. Process*. **27**, 2171–2186 (2013).

Acknowledgments: We would like to thank Katherine Richardson and Will Steffen for the discussions related to planetary boundaries, and the ISIMIP team and all participating modelling teams for making the outputs available.

Funding:

European Research Council (ERC) under the European Union's Horizon 2020 research and innovation programme (grant no. 819202) (MP, MK)

Erling-Persson Family Foundation (MP)

Aalto University School of Engineering Doctoral Programme (VV)

European Research Council through the "Earth Resilience in the Anthropocene" project (grant no. ERC-2016-ADG 743080) (LWE, IF, AT, JR)

IKEA Foundation (LWE)

Academy of Finland-funded project WATVUL (grant no. 317320) (MK)

The Netherlands Organization for Scientific Research (NWO), project number 016.Veni.181.015 (RvdE)

Author contributions:

Conceptualization: MP, VV, LWE, MK, DG, TG, CM, IF, FJ, AS, StW, AT, RvdE

Methodology: VV, MP, LWE, MK, DG, TG, CM, PD, MF, SNG, NH, YS, HMS, NW

Investigation: VV, MP, LWE, MK, DG, TG, CM

Writing – original draft: MP, VV, MK

Writing – review & editing: MP, VV with all authors

Visualization: VV, MP, MK

Supervision: MK, JR

Project administration: MP, VV, MK

Funding acquisition: MK, JR

Competing interests: Authors declare that they have no competing interests.

Data and materials availability: All data used in this study are gathered from openly available sources, which are appropriately cited in Materials and Methods. The code used in producing the results shown in this study will be deposited in a public database and released upon publication.

Supplementary Materials

Materials and Methods

Supplementary Text

Figs. S1 to S9

Table S1

References (39–75)

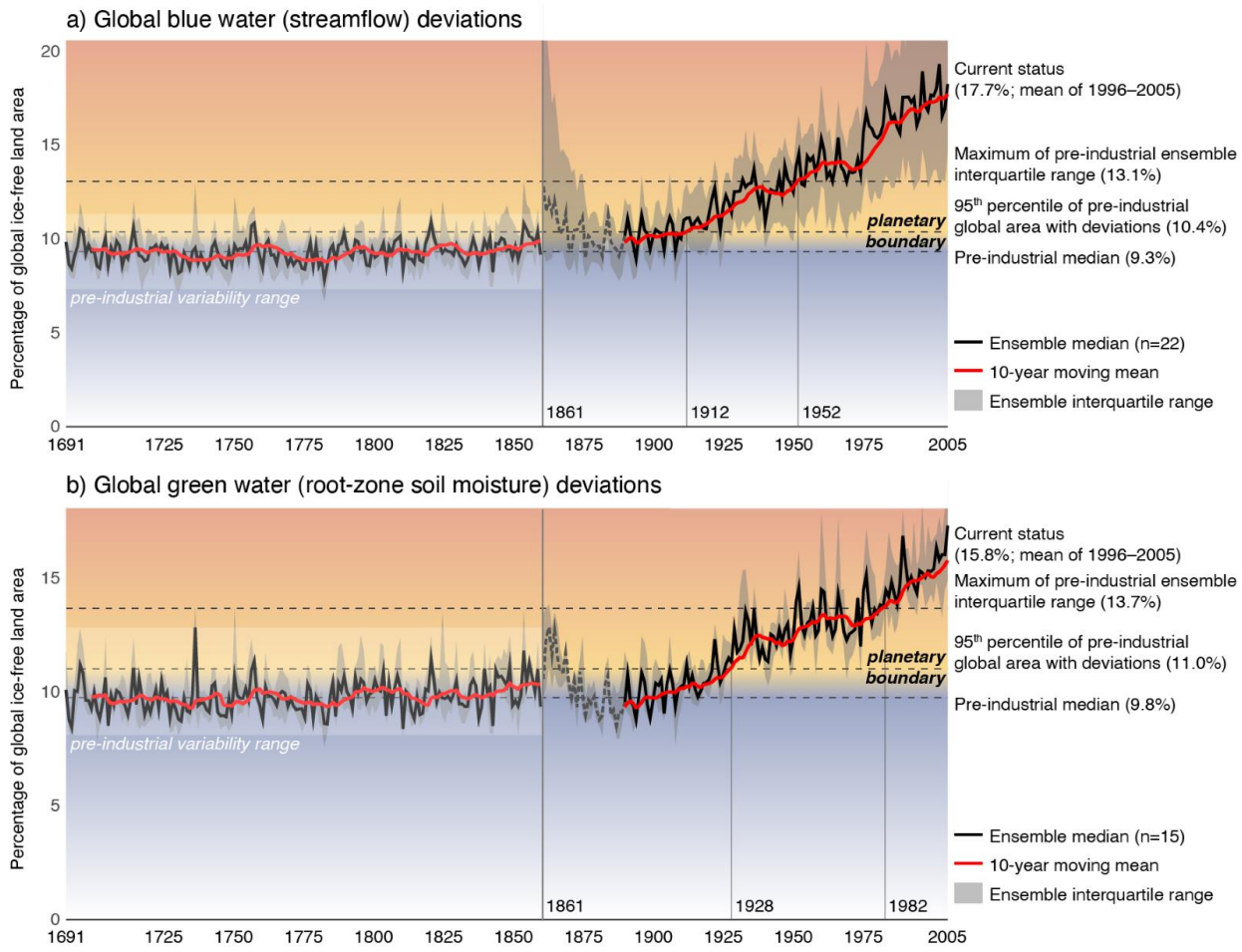

Fig. 1. Percentage of global ice-free land area with streamflow (a) and root-zone soil moisture (b) deviations from local (cell-wise) specific pre-industrial variability. Shown is the annual percentage, which is computed as an average of monthly values. The annotated years mark the 10-year moving (trailing) mean transgressing first the 95th percentile of the pre-industrial global area with deviations, and then the maximum of pre-industrial ensemble interquartile range. The ensemble median and interquartile range are computed from n = 22 (streamflow) and n = 15 (root-zone soil moisture) ensemble members. Values prior to 1691 are excluded and the ensemble median line for 1861–1890 is shaded and dashed due to traces of model spinups being common during these years (Fig. S2, S3) (*21*). Model-wise aggregates of percentage of land area with freshwater deviations are shown in Fig. S4 and Fig. S5.

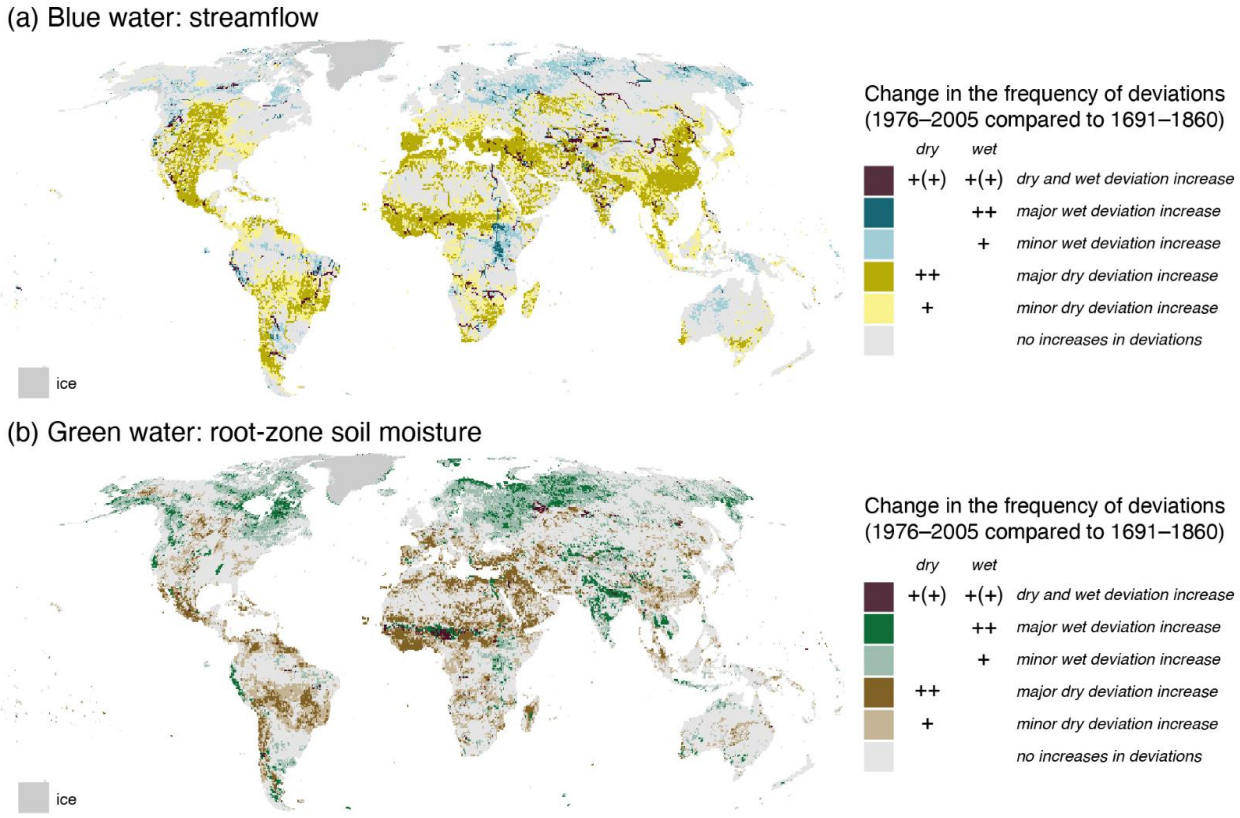

Fig. 2. Statistically significant increases in local (cell-wise) dry and wet deviations for blue water (a) and for green water (b). The changes are computed by comparing the ensemble median frequency of local deviations during 1976–2005 against 1691–1860, and significance of change ($p = 0.05$) is tested with R package stats function *prop.test* (*38*). Colors denoted with + indicate statistically significant increases with magnitude ≤5 pp (minor), whereas colors denoted with ++ indicate statistically significant increases with magnitude >5 pp (major). Colors denoted with +(+) pool together any statistically significant increase (minor or major).

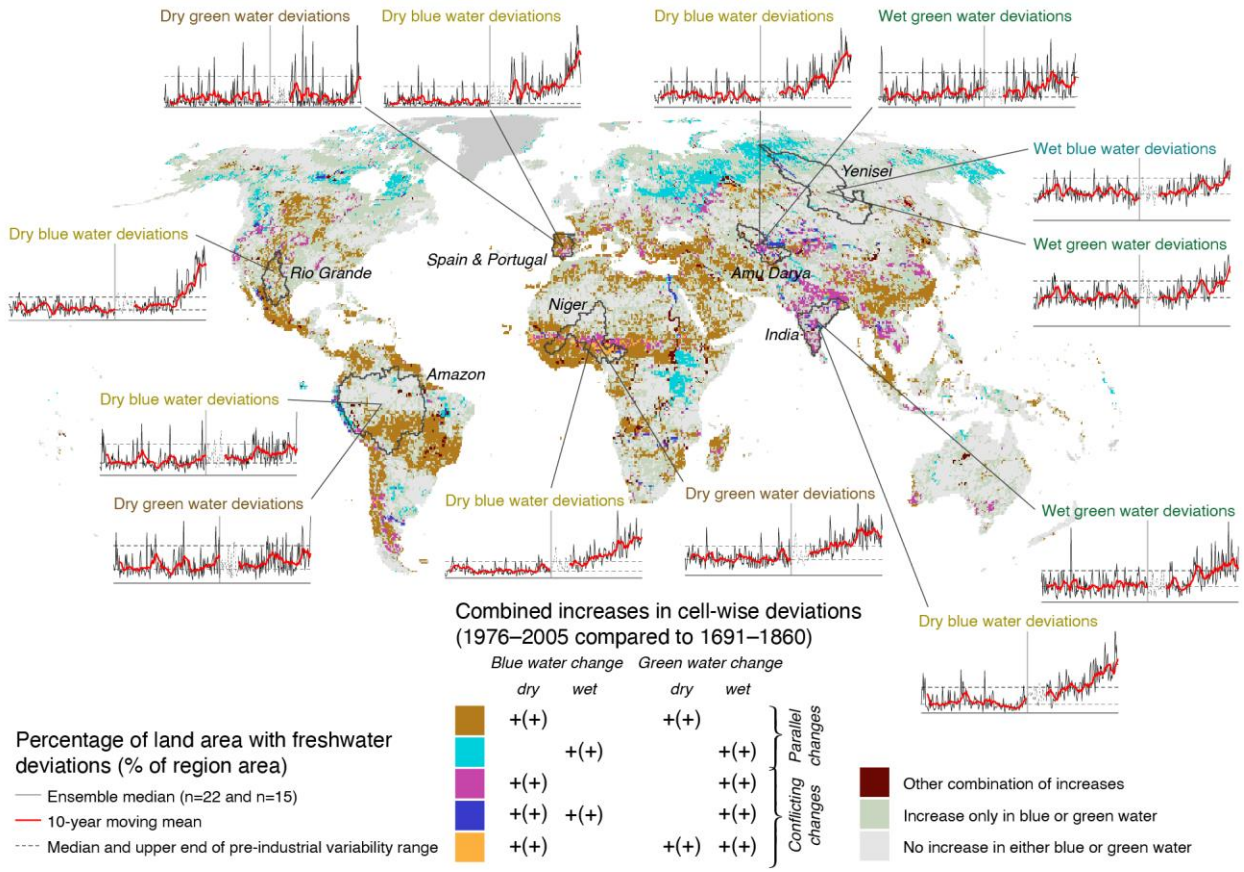

Fig. 3. Combined increases in local (cell-wise) deviations for blue and green water along with regional aggregates of dry or wet deviations in selected regions. Combination classes are based on deviation frequency increases presented in Fig. 2, and the main classes consist of both blue and green water changes (minor or major; represented by +(+) in the legend). Changes in only one or neither are colored in lighter colors. Land area aggregation is performed within each region, and the median and 95th percentile of pre-industrial area with deviations are also computed regionally.

Supplementary Materials for

Global water cycle shifts substantially beyond stable pre-industrial conditions

Miina Porkka†, Vili Virkki†, Lan Wang-Erlandsson, Dieter Gerten, Tom Gleeson, Chinchu Mohan, Ingo Fetzer, Fernando Jaramillo, Arie Staal, Sofie te Wierik, Arne Tobian, Ruud van der Ent, Petra Döll, Martina Flörke, Simon N. Gosling, Naota Hanasaki, Yusuke Satoh, Hannes Müller Schmied, Niko Wanders, Johan Rockström, Matti Kummu

†These authors contributed equally to this work
Correspondence to: miina.porkka@aalto.fi, vili.virkki@aalto.fi

This PDF file includes:

Materials and Methods

In comparing historical and pre-industrial states of the freshwater cycle, we followed the general approach of Wang-Erlandsson et al. (*20*) with certain changes related to data and methodology. First, instead of custom runs using the global dynamic vegetation model LPJmL 5.1 forced with bias-corrected and downscaled CMIP6 climate data (*20*), we used the ISIMIP 2b global hydrological model outputs that are forced with bias-corrected climate data from CMIP5 (*39*). Second, we chose to define the grid cell scale local pre-industrial bounds strictly cell-wise and performed annual aggregation by monthly averaging. Both of these changes are further detailed in the following sections. In the following sections, we first explain the selection of hydrological variables and baseline conditions, then describe the data and the method of calculating freshwater change. The main steps of our analysis are presented in Figure S1.

Control variables and baselines of freshwater change

Due to different and sometimes competing functions of different elements of the water cycle, we divided the freshwater change analysis into green and blue water components. For green water, we followed Wang-Erlandsson et al. (*20*) who suggested, after an extensive literature review, that root-zone soil moisture is the most suitable control variable for representing the Earth system functions of green water. For blue water, we selected river streamflow as the control variable to represent its Earth system functions. Streamflow alterations are either directly or indirectly connected to many major anthropogenic modifications of blue water stocks and flows, including e.g. water withdrawals, flow regulation, and groundwater depletion, as well as many key Earth system functions of blue water, such as aquatic habitat provision and storage and transport of carbon and nutrients (*1*). Furthermore, streamflow is impacted by anthropocentric climate change (*40*). We therefore consider it to reasonably represent blue water change, though acknowledging its limitations, such as only partially reflecting groundwater changes and their Earth system impacts. In addition to an adequate representation of the human drivers and Earth system impacts of freshwater change, the selected control variables are routinely simulated by global hydrological models and can therefore be updated on an annual basis. The variables can, in principle, also be observed directly, e.g. by in situ measurements or remote sensing (*41*, *42*), though spatial and temporal coverage of observational data is currently not sufficient for a comprehensive global analysis such as the one presented here.

The planetary boundaries framework (*7*, *8*) refers to the Holocene geological epoch as the desired baseline conditions. However, as major spatial shifts of the water cycle have occurred since the Holocene (*43*, *44*), strictly grid cell scale comparisons – as those done here – are not feasible. Hence, we selected the pre-industrial period as our comparison baseline, also because of the wide availability of consistent and comparable ISIMIP 2b data (*39*). By grounding our analysis in the pre-industrial period, we were able to establish our baseline before substantial anthropogenic modifications of the water cycle, including e.g. large dams (*27*), large scale irrigation systems (*26*), the rapid increase of intensive land uses (*45*), and anthropocentric climate change (*40*). Therefore, we presumed that the pre-industrial period adequately represents Holocene-like conditions – and that widespread deviations from that ‘pristine’ state are problematic.

Data selection

Our main data source was the Inter-Sectoral Impact Model Intercomparison Project (ISIMIP) data repository (available at: https://data.isimip.org, last accessed July 1st, 2022), from

which we took data from the ISIMIP 2b simulation round experiments (*39*). We used root-zone soil moisture (hereafter soil moisture; ISIMIP output variable *rootmoist*) for green water and river discharge (hereafter streamflow; ISIMIP output variable *dis*) for blue water.

Two distinct simulation scenarios were required to set the pre-industrial baseline and compare the historical state of the water cycle to it. For the pre-industrial period, we used model outputs forced with *picontrol* climate and *1860soc* land use and socio-economic conditions, and at the transition from pre-industrial to historical simulations in 1860, we switched to *historical* climate combined with *histsoc* land use and socio-economic conditions (*39*). Hence, our pre-industrial baseline was established with a constant 286 ppm CO_2 concentration and fixed pre-industrial land use and socio-economic conditions, whereas carbon-induced climate change and human influences (e.g. land use change, water use, and dam operation) are represented in our data during the historical period.

Soil moisture and streamflow were simulated by global hydrological models (GHMs), which in this case were forced with bias-adjusted output of modelled climate from general circulation models (GCMs). The GCM outputs from CMIP5 (*46*) were bias-adjusted with an observational dataset covering the years 1979–2013 (*39*). From the ISIMIP 2b repository, we selected all GHM-GCM combinations, for which output data were available for both *picontrol-1860soc* and *historical-histsoc* scenarios (Table S1). For soil moisture, outputs from four GHMs (CLM50 (*47*), LPJmL (*48*), MPI-HM (*49*), and PCR-GLOBWB (*50*)) were available by these criteria, and correspondingly for streamflow, outputs from six GHMs (H08 (*51*), LPJmL, MATSIRO (*52*), MPI-HM, PCR-GLOBWB, and WaterGAP2 (*53*)) were available. For all GHMs, four GCMs were available: GFDL-ESM2M (*54*), HadGEM2-ES (*55*), IPSL-CM5A-LR (*56*), and MIROC5 (*57*), with the exception of MPI-HM, which lacked HadGEM2-ES for both variables. In addition, data files for *picontrol-1860soc* streamflow simulation for MATSIRO-HadGEM2-ES were incomplete, which led us to discard this combination. Hence, our soil moisture data ensemble consisted of 15 members (GHM-GCM combinations) and our streamflow data ensemble consisted of 22 members.

The ISIMIP 2b data is archived so that pre-industrial years range from 1661 to 1860 and the historical years from 1861 to 2005. The pre-industrial simulation years are, however, nominal, as the CMIP5 data used to force ISIMIP 2b models represent 200 control years with climate variability at pre-industrial levels (with no correspondence to the actual weather of individual years) (*39*). The temporal coverage of historical simulations ends in 2005 owing to estimates of e.g. irrigation extent not being available (*26*). For streamflow, we aggregated daily values to monthly values by taking the mean of daily streamflow, whereas soil moisture data were readily delivered in monthly time resolution. The spatial resolution of all data was 0.5 degrees (ca. 50x50 km at the Equator). The models in ISIMIP 2b have often been validated against observations, showing adequate performance especially when estimates from individual models are combined in an ensemble modelling approach (*58–61*). As we construct ensembles as large as possible, given the availability of different scenarios, we can partially tackle the uncertainty to which global modelling is always subject to a certain degree (*62*).

Data preparation

Because the data we used originates in two different scenarios, and the ISIMIP simulations can be run independently of each other, we had to ensure that the simulations are harmonized. If the simulations are not continuous, the end state of the pre-industrial simulation does not necessarily equal the initial state of the historical simulation at the grid cell scale. Due to this, two main kinds of discontinuities may arise: 1) traces of model spinup, which are caused by the GHM reaching an equilibrium in terms of water storage but only after a certain period after the

beginning of the simulation and 2) shifts in value distribution around the transition point at 1860 (e.g. abrupt shift in the moving mean or disturbance in local linear trends). Further, a combination of the former two is also possible. Fig. S2 shows an example of traces of model spinup, whereas Fig. S3 shows our general approach to ensure the fit between the simulation periods along with an example of a cell in which the value distribution shifts. We performed the spinup detection (Fig. S2) and the shift correction (Fig. S3) separately for each grid cell, month, and ensemble member.

First, we checked for any traces of spinups by detecting the most likely changepoint in the mean and variance of the data with function *cpt.meanvar* in R package *changepoint* (*63*, *64*), separately for the pre-industrial and historical periods. As the spinup is related to the hydrological state in a cell reaching an equilibrium, we assumed that a trace of spinup is located between 10 and 30 years after the initiation of each simulation period, as is the case in Fig. S2, for example. Outside this period, we considered that changepoints were true (natural) changes in mean and variance, and did not imply a trace of spinup in the data. If a changepoint was detected within the above-mentioned period, all data before the changepoint were discarded from correcting the distribution shifts. Otherwise, the ten first years were discarded, as shown in Fig. S3, in which spinups are detected either before 10 years or after 30 years from the initiation. Depending on the month and ensemble member, the changepoints indicating traces of spinup were detected in 1.4–8.7% (pre-industrial streamflow), 1.6–7.2% (historical streamflow) 0.4–4.6% (pre-industrial soil moisture), and 0.6–5.7% (historical soil moisture) of all cells.

We checked and corrected the shifts in value distribution around 1860 with an iterative technique that combined linear extrapolation and quantile mapping. First, we needed to extrapolate the pre-industrial data onto the historical simulation period, as the simulation periods have no temporal overlap, and cell-wise trends are possible also during the pre-industrial period (Fig. S3a). This was done by fitting a linear regression model (*65*) to pre-industrial values excluding spinup (i.e. 1671–1860 in most cases, with flexibility of starting from 1691 at latest), and extrapolating the linear trend to the historical period (blue lines in Fig. S3a). Further, we computed the standard deviation of the pre-industrial values to which the linear model was fit (defined here as σ_{preind}), and added normally distributed random noise ($\mu = 0$, $\sigma = \sigma_{preind}$) to the linear extrapolation (blue circles in Fig. S3a).

After extrapolation, we fitted non-parametric quantile mapping using robust empirical quantiles implemented in R package *qmap* (*66*, *67*) between the historical simulation values and the extrapolated pre-industrial values. Four quantiles were used in fitting the quantile mapping. Here, we treated the historical values as 'observed' data and the extrapolated pre-industrial values as 'modelled' data, although both are simulated GHM outputs. We chose to fit the quantile mapping between 30 years of historical and extrapolated pre-industrial values, starting from the first year not excluded after spinup detection. Hence, for most cells, quantile mapping was fitted using years 1871–1900 as the 'observed' values with flexibility of extending the fitting period to 1891–1920 at maximum. For example, the fitting period for the cell shown in Fig. S2 was 1874–1903, whereas for the cell shown in Fig. S3, the fitting period was 1871–1900. Although 30 years is a relatively short period, and some spinups might end only after 1891, we chose to limit the quantile mapping with these years to prevent the historical values being substantially affected by anthropogenic impacts, which becomes more likely during the early 20th century.

Finally, pre-industrial values excluding spinup were transformed with the fitted quantile mapping function (Fig. S3b). However, as the quantile mapping was based on extrapolation and a relatively small sample size, distinctive individual values or undetected traces of spinup might have distorted the quantile mapping function. Hence, we checked whether correcting the

distribution shifts succeeds in improving the fit between the simulation periods. To do this, we ran our analysis up until detecting cell-wise deviations from the local pre-industrial bounds (see next section for details) – first without correction and then with correction – and consequently checked whether the deviations from the local pre-industrial bounds decrease owing to the correction. Checking the deviations was performed for a period of 50 years beginning from the first year not excluded after spinup detection. This was to include data also beyond the period which was used in fitting the quantile mapping. Should the number of deviations from the local pre-industrial bounds decrease, we considered that our procedure had improved the fit between the simulation periods and the corrected cell values were accepted, otherwise we discarded the corrected data and retained the uncorrected data. Globally, depending on month and ensemble member, the correction was accepted for approximately 10–29% of soil moisture cells and 6–26% of streamflow cells (except for H08, for which all cells were corrected).

Identifying local deviations

We defined the 5th and 95th percentiles of pre-industrial streamflow and soil moisture as the local pre-industrial bounds of normal variability, separately for each grid cell, month, and ensemble member (Fig. S1a, b). The definition of local pre-industrial bounds differs from Wang-Erlandsson et al. (*20*) who drew the 5th and 95th percentiles from the values in a grid cell and its eight neighboring grid cells. We chose to be stricter in this definition because using a neighborhood in determining the local pre-industrial bounds can potentially set them unrealistically wide – especially in the case of streamflow. Spinups were excluded from drawing the local pre-industrial bounds, which means that for most cells, the bounds were drawn from 190 values covering the years 1671–1860, though allowing flexibility up until 1691 (e.g. in Fig. S2, the local bounds were drawn from 1690–1860). Then, again for each grid cell, month, and ensemble member, we checked for all pre-industrial months whether streamflow or soil moisture would fall within or outside the local pre-industrial bounds. Should the monthly value be lower than the local dry bound (5th percentile), this month was marked as a dry deviation, while in cases of the monthly value surpassing the local wet bound (95th percentile), the month was marked as a wet deviation (Fig. S1c). Deviations from local pre-industrial bounds were evaluated for all values including spinups, and all deviations were determined as binary (deviation/no deviation) with no regards to deviation magnitude.

Calculating global indicators

After determining the local deviations from pre-industrial bounds, we aggregated (summed) the physical areas of cells with dry and wet deviations, separately for each month and ensemble member (Fig. S1d). We excluded Antarctica and other permanent land ice using anthromes from HYDE 3.2.1 (*68*) and divided the area with deviations by total ice-free land area to yield *the percentage of ice-free land area with streamflow or soil moisture deviations from pre-industrial variability*. We transformed the monthly percentages into annual percentages by taking the annual means of the monthly percentages (Fig. S1d). This differs from Wang-Erlandsson et al. (*20*) who marked an individual grid cell annually deviating if a deviation from the local pre-industrial bounds occurred during any month of the year, and subsequently aggregated global land area only annually. We chose to aggregate areas monthly to distinguish between cases in which deviations occur during only one month or many months within a year – i.e. when freshwater change is temporally less or more extensive. With our approach, more frequent deviations have a higher impact on the annual average of monthly shares of land areas.

As approximately 5% of all pre-industrial values in each grid cell are outside of the local dry and wet pre-industrial bounds by definition (5th/95th percentile), the expected share of global

land area with deviations (under stable conditions) is also approximately 5% per dry and wet bound. Hence, summing both dry and wet bounds together, deviations are expected in roughly 10% of global ice-free land area but with some natural variation. As spinups are prevalent especially in some models (Fig. S5, S6), global percentages prior to 1691 were excluded from further analysis. Finally, we determined the ensemble (n = 15 or n = 22) median and interquartile range of the global percentage (Fig. S1e). This resulted in a time series of n = 170 when excluding values prior to 1691.

The ensemble median time series (n = 170) of the percentage of ice-free land area with streamflow or soil moisture deviations characterized *the global pre-industrial variability range*, from which we defined two main metrics: the median and the upper end. *The median of pre-industrial variability range* was defined as the 50th percentile of the ensemble median time series, while *the upper end of the pre-industrial variability range* was defined as the 95th percentile of the ensemble median time series (Fig. S1e, f). Hence, the median describes the typical percentage of land area with freshwater deviations during the pre-industrial (Holocene-like) conditions, whereas the upper end describes conditions that occur expectedly once in every 20 years. For underpinning scientific uncertainty, we also marked the maximum of pre-industrial ensemble interquartile range to be compared against. Should the historical percentages partially or completely exceed the pre-industrial ensemble interquartile range, it is more likely in the sense of uncertainty that the area with streamflow or soil moisture deviations has increased.

To assess the historical (1861–2005) state of the water cycle, we repeated the estimation of local deviations and global aggregation of the area with streamflow or soil moisture deviations (Fig. S1g), and compared that to the pre-industrial variability range (Fig. S1h). Again, we included all years in evaluating the local deviations, but we chose to shade years 1861–1890 in the figures that show global percentages owing to the spinups being prevalent in some models (Fig. S4, S5). Further, we took the ensemble median of the global percentage also for the historical time period and applied a moving (trailing) 10-year mean over this ensemble median line, with the latest 10-year mean (for year 2005, computed as a mean of values from 1996–2005) being defined as the *current status*.

Supplementary Text

Limitations and uncertainties

While our analysis advances the previous freshwater PB assessments in many respects, a number of limitations and uncertainties remain to be tackled in the future. Our estimate of the 'current' status of global freshwater change ends in 2005, due to the ISIMIP 2b simulation protocol. In the 15–20 years since the end of our study period, global trends in many of the key drivers of freshwater change, such as irrigated area (*69*), water use (*70*), dam construction (*71*) and forest loss (*72*), have increased. Hence, the latest estimates presented here are likely conservative, and a substantial further transgression of the PB during the more recent years can be assumed.

Specific to our data, it is known that global hydrological models are relatively sensitive to their internal implementation of anthropogenic drivers and impacts (*59*, *62*) and sometimes perform poorly under certain conditions (*73*). Also, although the ISIMIP 2b simulations use state-of-the-art input data and consistent scenario definitions, the different process descriptions of GHMs lead to a considerable spread in our data ensemble (Fig. S4, S5). Resulting from these, our global – and especially local – results are subject to uncertainty, considering also the relatively prevalent discontinuities in data that we corrected for the purposes of this analysis. As our scenario setup of using dynamic *histsoc* socio-economic conditions against static *1860soc*

(Table S1) already implies a change in anthropogenic water cycle impacts, it is not an unexpected result that aggregate changes in the water cycle are manifested early during the 20th century. Repeating the analysis with data that would be absent of anthropogenic forcing (ISIMIP *nosoc* scenarios) (*39*) would potentially aid in estimating how large proportions of freshwater changes are due to indirect (e.g. climate change) vs. direct (e.g. water use) anthropogenic factors, but models that would have been run for both *picontrol-1860soc* (or *picontrol-nosoc*) and *historical-nosoc* scenarios are not available in ISIMIP 2b. However, despite the related uncertainties, our approach is globally as coherent as the current knowledge and modelling capacities allow. Moreover, the magnitude and rate of global freshwater change in the historical period and the likely underestimation of its current status suggest that our conclusion of the freshwater cycle substantially transgressing its "natural" variability range is valid. Future modelling efforts (e.g. ISIMIP simulation round 3; https://www.isimip.org/protocol/3/, last access July 1st, 2022) could provide an excellent opening to further develop our analysis.

Moreover, the selected hydrological variables do not represent all freshwater changes – such as water quality aspects – and omit explicit consideration of other freshwater flows and stocks, e.g. groundwater and land ice. From the perspective of the PB framework, however, these choices can be justified, as water quality is (implicitly) considered in the PBs of Biogeochemical flows and Novel entities (*7*, *8*), and because such an overarching framework requires expressing very complex Earth system processes in relatively simple terms. Nonetheless, a more comprehensive assessment of humanity's overall impact on the freshwater cycle would require careful consideration of the many complex relationships between drivers, hydrological responses and their Earth system impacts that weren't explicitly considered in this analysis.

Major uncertainties remain also regarding the planetary boundary value of freshwater change – that is, which level of freshwater alteration would trigger state changes in the Earth system. Although impacts of freshwater change on the Earth system functions of freshwater have been studied extensively at local to regional scales (*1*), regional to planetary scale assessments of impacts are still lacking. Furthermore, the PBs' control variables – including freshwater – interact strongly with each other, which should be considered when setting a PB for freshwater change (*35*). These factors complicate the boundary setting, as ideally, PBs should be set based on control variable–response variable relationships to minimize the risk of abrupt or irreversible state shifts. In the absence of such assessments, we chose to set the boundary at the upper end of the pre-industrial, Holocene-like variability range, as it represents conditions that were present before major anthropogenic alterations and can therefore be considered safe. It is possible, however, that the intrinsic resilience of the Earth system will maintain a Holocene-like state even if the pre-industrial range of variability is exceeded – as it has already been for a long time. However, as the extent of a 'safe' exceedance cannot be robustly defined without quantifications of Earth system-wide responses of freshwater change, we applied the precautionary principle of the PB framework (*8*, *74*), and set the boundary at what we consider to be the lower end scientific uncertainty.

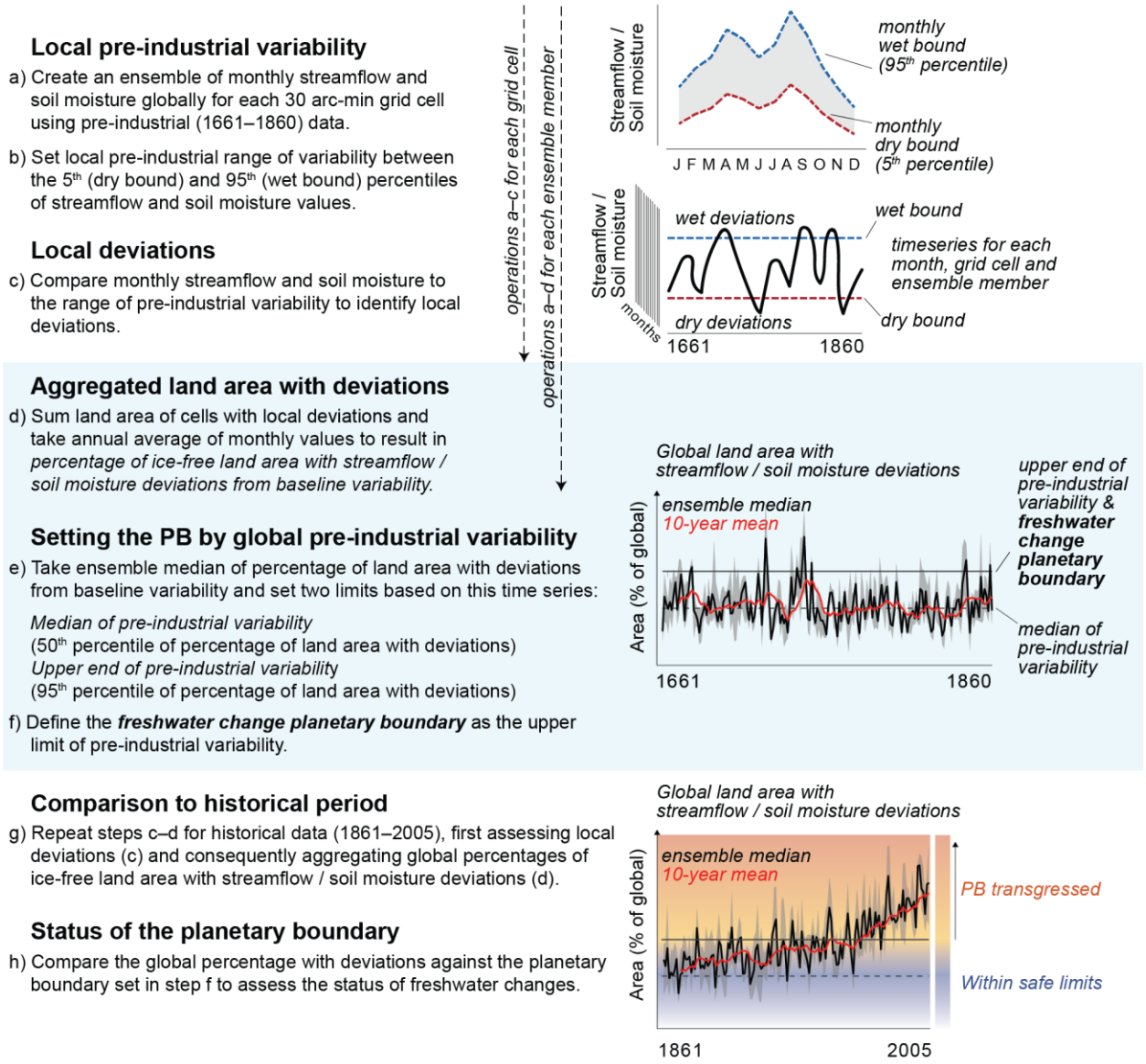

Fig. S1.

Methodological outline of the study; establishing and assessing the status of freshwater change planetary boundary. The steps a–h are described in detail in Materials and Methods.

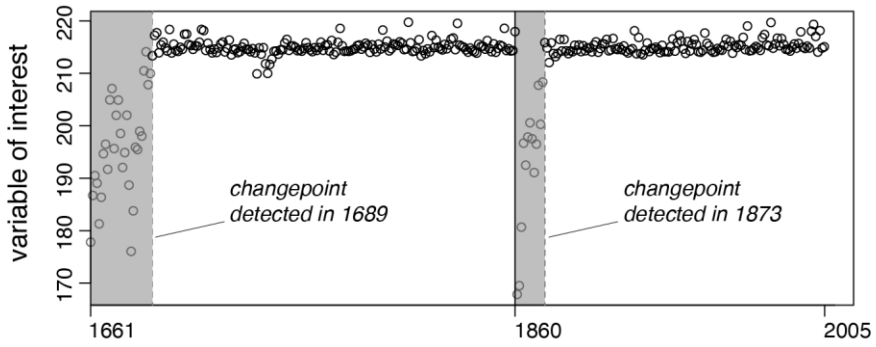

Fig. S2.

An example case of detecting the most likely changepoints in mean and variance. The values shown in the plot describe soil moisture in one grid cell, for one month, and for one ensemble member. As the changepoints are detected between 10 and 30 years from the initiation of each period, they are considered as traces of model spinup. Hence, values shaded in grey are excluded from distribution shift correction (Fig. S3) and consequently determining the local pre-industrial bounds.

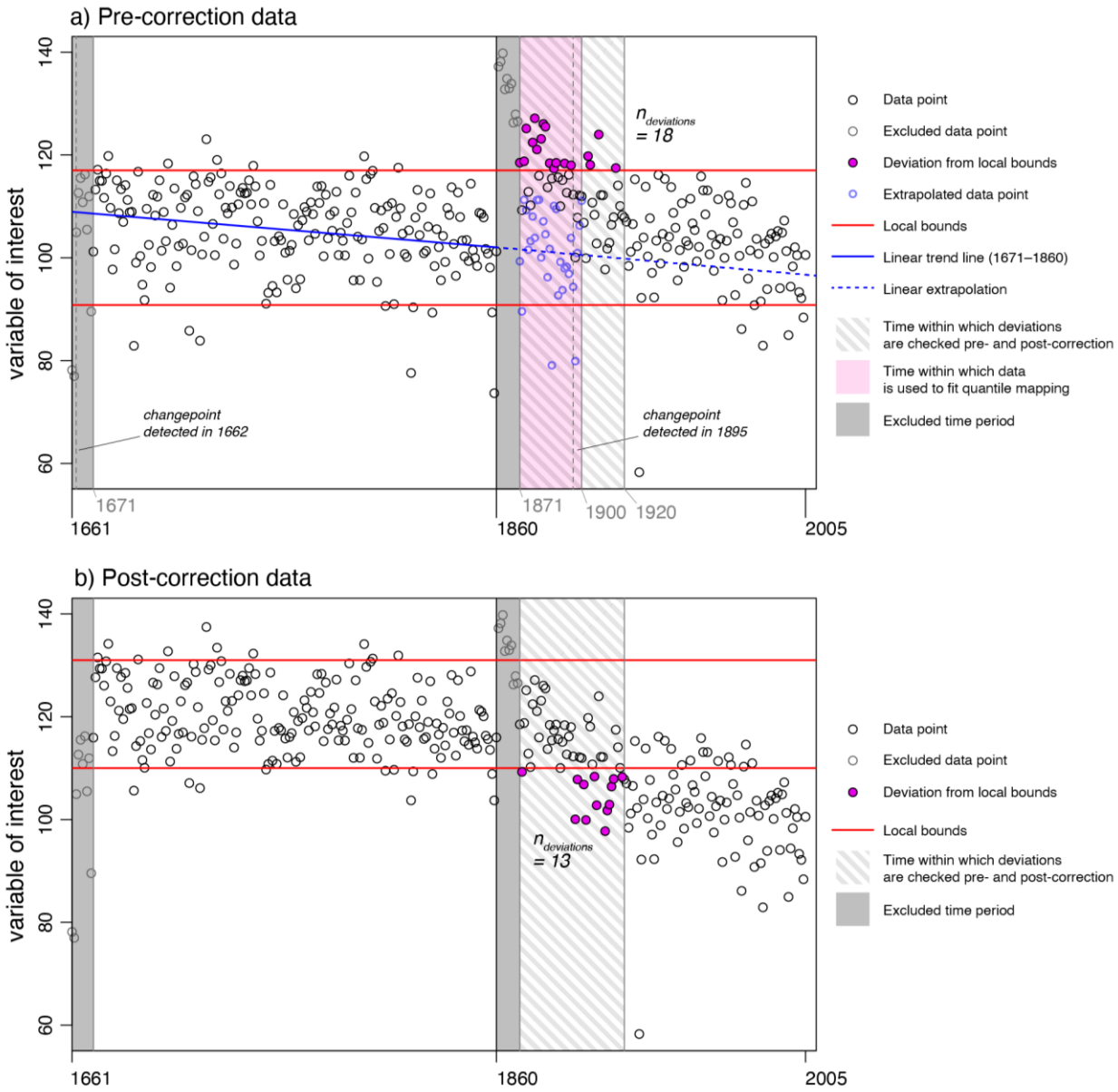

Fig. S3.

Correcting shifts in cell-wise value distribution around the year 1860 transition point between pre-industrial and historical ISIMIP 2b simulations. The values shown in the plot describe soil moisture in one grid cell, for one month, and for one ensemble member. Black circles show data prior to correction (a) and after the correction (b). Linear trend (blue line) is estimated and extrapolated excluding the ten first pre-industrial values (i.e. for 1671–1860). For a time period highlighted with magenta shading, quantile mapping is fitted between historical simulation values and the extrapolated values that are added with random normal noise (blue circles). Once quantile mapping is applied for pre-industrial data, resulting in panel b, the number of deviations (purple filled circles) from local bounds (red lines) is compared pre- and post-correction for a period of 50 years (striped shading). Should the number of deviations decrease, as is the case here, the corrected values (panel b) are accepted, otherwise the uncorrected values (panel a) would be retained.

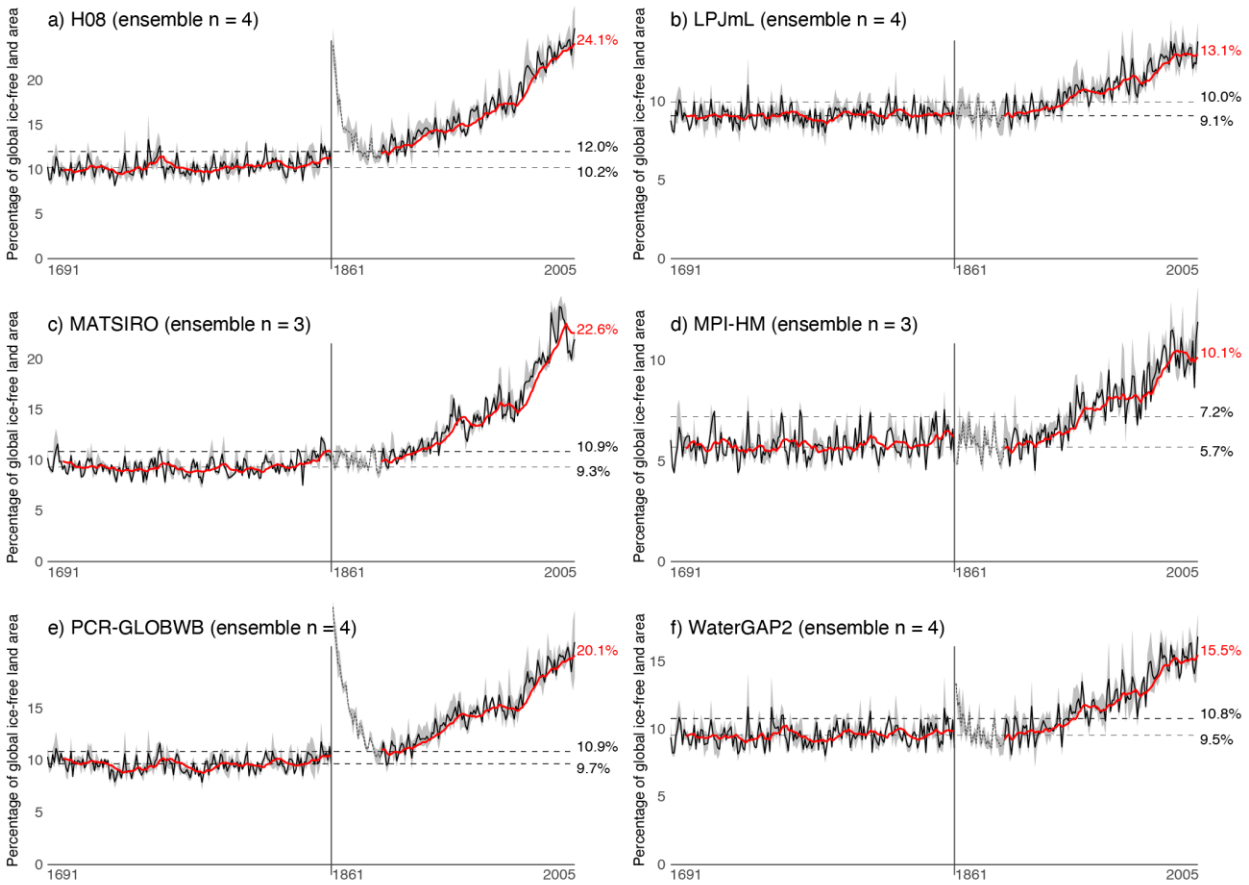

Fig. S4.

Percentage of global ice-free area with streamflow deviations from local (cell-wise) specific pre-industrial variability, separately for global hydrological models (GHMs) included in this study: H08 (a), LPJmL (b), MATSIRO (c), MPI-HM (d), PCR-GLOBWB (e), and WaterGAP2 (f). Shown is the annual percentage, which is computed as an average of monthly values. The vertical lines drawn in each panel denote the median and the upper end of the pre-industrial variability range, and the current status is annotated at the end of the red 10-year moving (trailing) mean line. The ensemble median and interquartile range are computed from n = 3–4 members (number of GCMs), as data forced with HadGEM2 were not available for MATSIRO and MPI-HM. The ensemble median line for 1861–1890 is shaded and dashed due to traces of model spinups being common during these years (especially a, e, f).

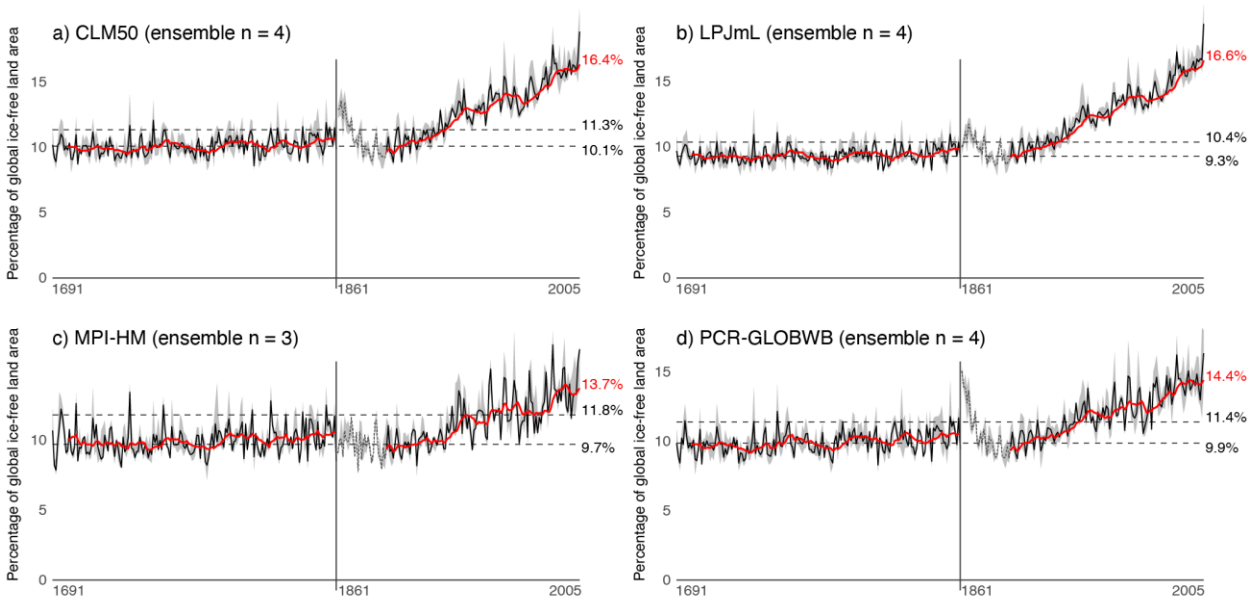

Fig. S5.

Percentage of global ice-free land area with soil moisture deviations from local (cell-wise) specific pre-industrial variability, separately for global hydrological models (GHMs) included in this study: CLM50 (a), LPJmL (b), MPI-HM (c), and PCR-GLOBWB (d). Shown is the annual percentage, which is computed as an average of monthly values. The vertical lines drawn in each panel denote the median and the upper end of the pre-industrial variability range, and the current status is annotated at the end of the red 10-year moving (trailing) mean line. The ensemble median and interquartile range are computed from n = 3–4 members (number of GCMs), as data forced with HadGEM2 was not available for MPI-HM. The ensemble median line for 1861–1890 is shaded and dashed due to traces of model spinups being common during these years (especially a, d).

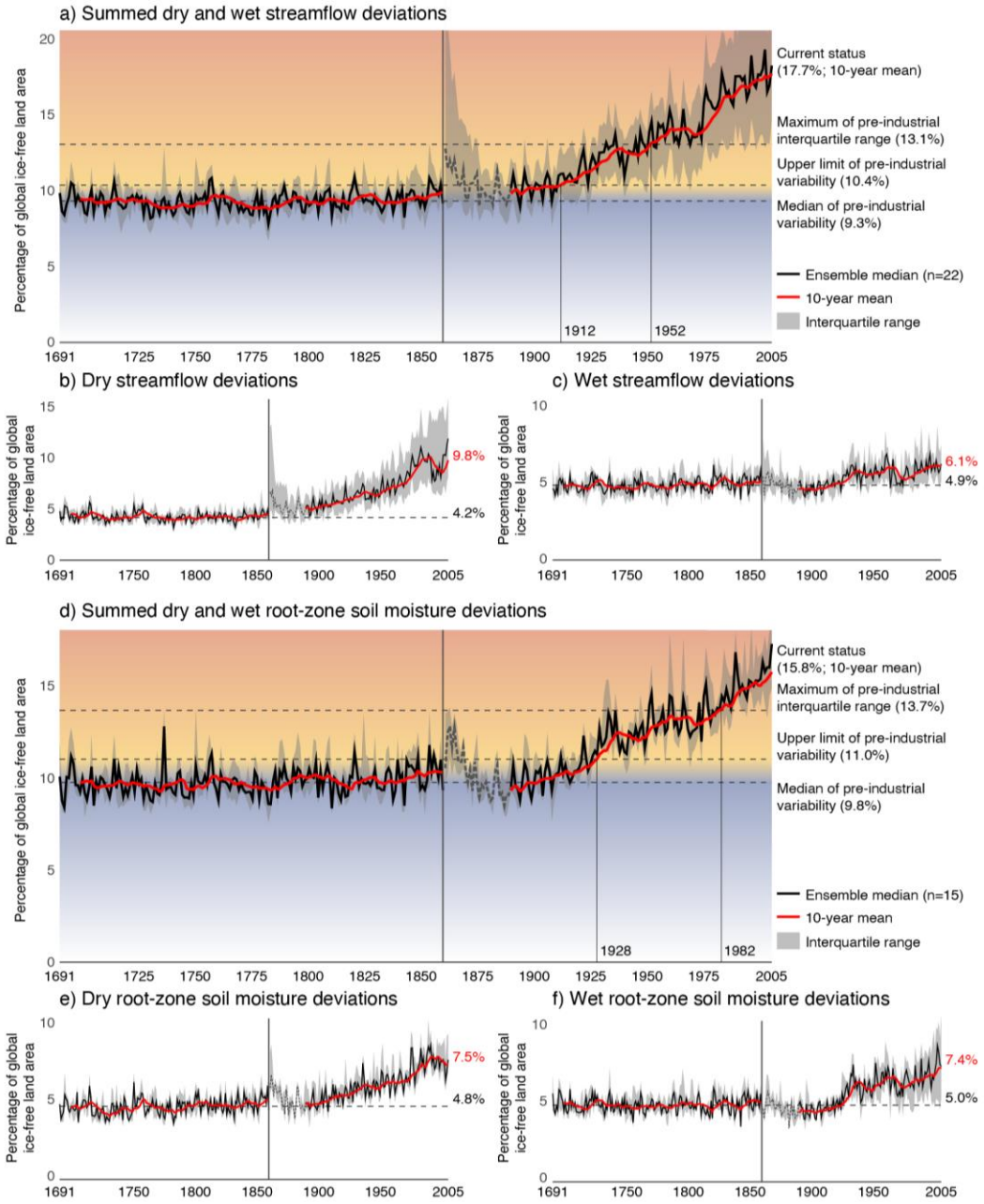

Fig. S6.

Percentage of global ice-free land area with streamflow (a–c) and soil moisture (d–e) deviations from local (cell-wise) specific pre-industrial variability, dry and wet deviations summed (a, d), and for dry (b, e) and wet (c, f) deviations separately. Shown is the annual percentage, which is computed as an average of monthly values. The annotated years mark the 10-year moving (trailing) mean transgressing first the 95th percentile of the pre-industrial global area with deviations, and then the maximum of pre-industrial ensemble interquartile range. The ensemble median and interquartile range are computed from n = 22 (streamflow) and n = 15 (soil moisture) ensemble members. The ensemble median line for 1861–1890 is shaded and dashed due to traces of model spinups being common during these years (Fig. S2, S3). The apparent dip in dry streamflow deviations (b) during the late 20th century is a product of the MATSIRO model (i.e. 3 ensemble members).

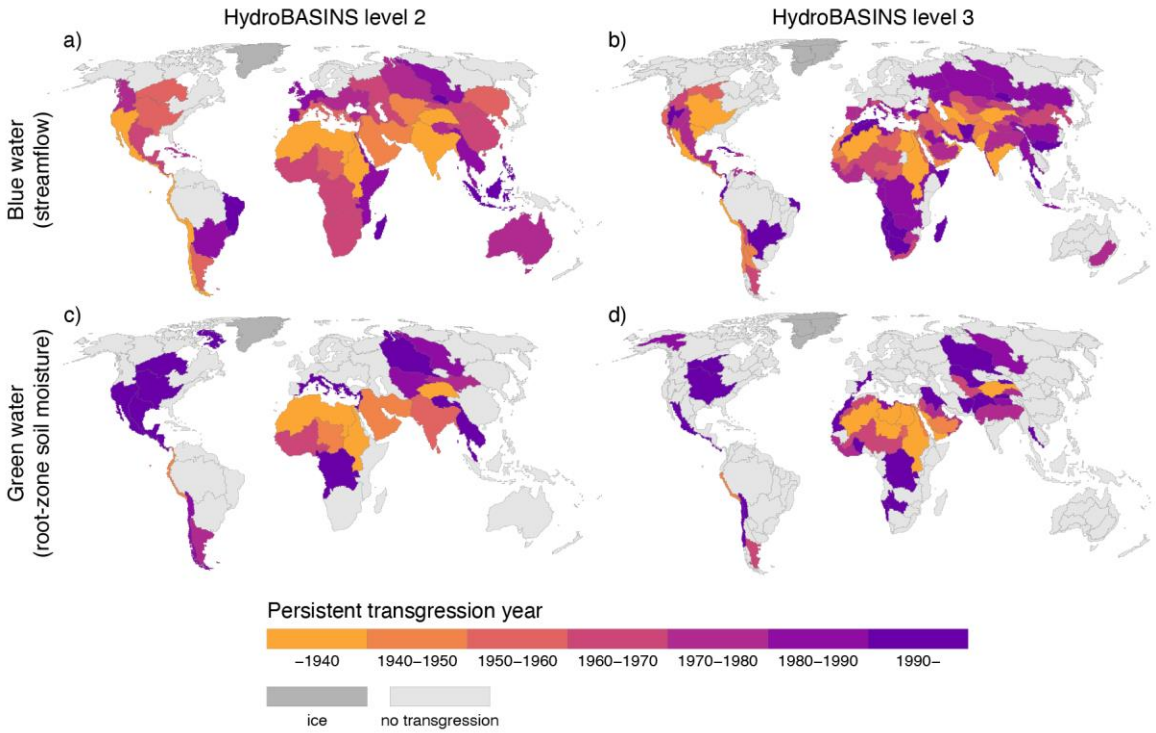

Fig. S7.

Time of regional persistent transgression of the upper end of pre-industrial variability range, for blue water (a–b) and green water (c–d). Here, cell-wise deviations are first aggregated regionally to get a percentage of area with streamflow or soil moisture deviations, then the upper end of the pre-industrial variability range is set to the 95th percentile of pre-industrial percentage with deviations, and finally the historical period is compared against the pre-industrial period. The persistent transgression year is defined as the first year, during which the 10-year moving (trailing) mean of percentage with deviations has exceeded the region-specific upper end of pre-industrial variability range for ten consecutive years, and the 10-year moving mean does not return below the upper end of pre-industrial variability range after this year. The regions shown here depict basins delineated by the HydroBASINS data set level 2 (a, c; n = 60, mean area = 2,247,000 km^2, median area = 2,045,000 km^2) and level 3 (b, d; n = 264, mean area = 511,000 km^2 median area = 313,000 km^2) (*75*).

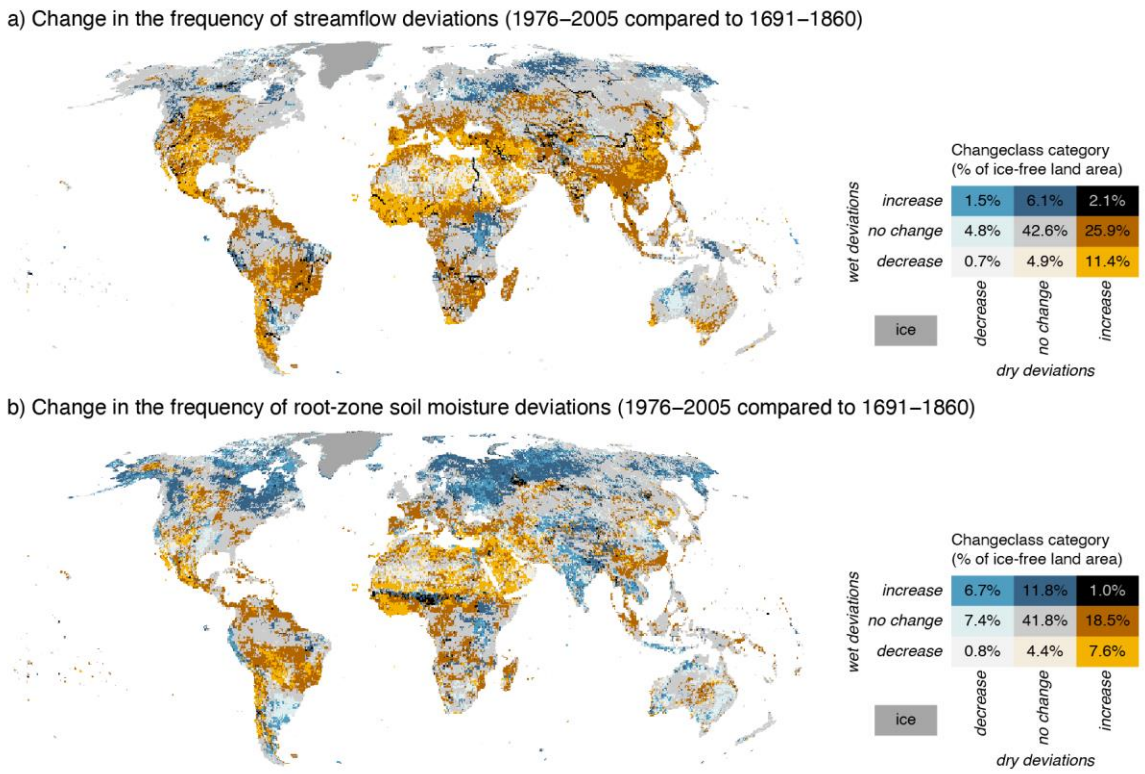

Fig. S8.

Statistically significant changes in local (cell-wise) dry and wet deviations for blue water (a) and for green water (b). The changes are computed by comparing the ensemble median frequency of local deviations during 1976–2005 against 1691–1860, and significance of change (p = 0.05) is tested with R package *stats* function *prop.test* (*38*). The changes are classified according to the direction of change (decreasing or increasing frequency of deviations) but with no regards to magnitude. Land area covered by each class is represented in the bivariate legend.

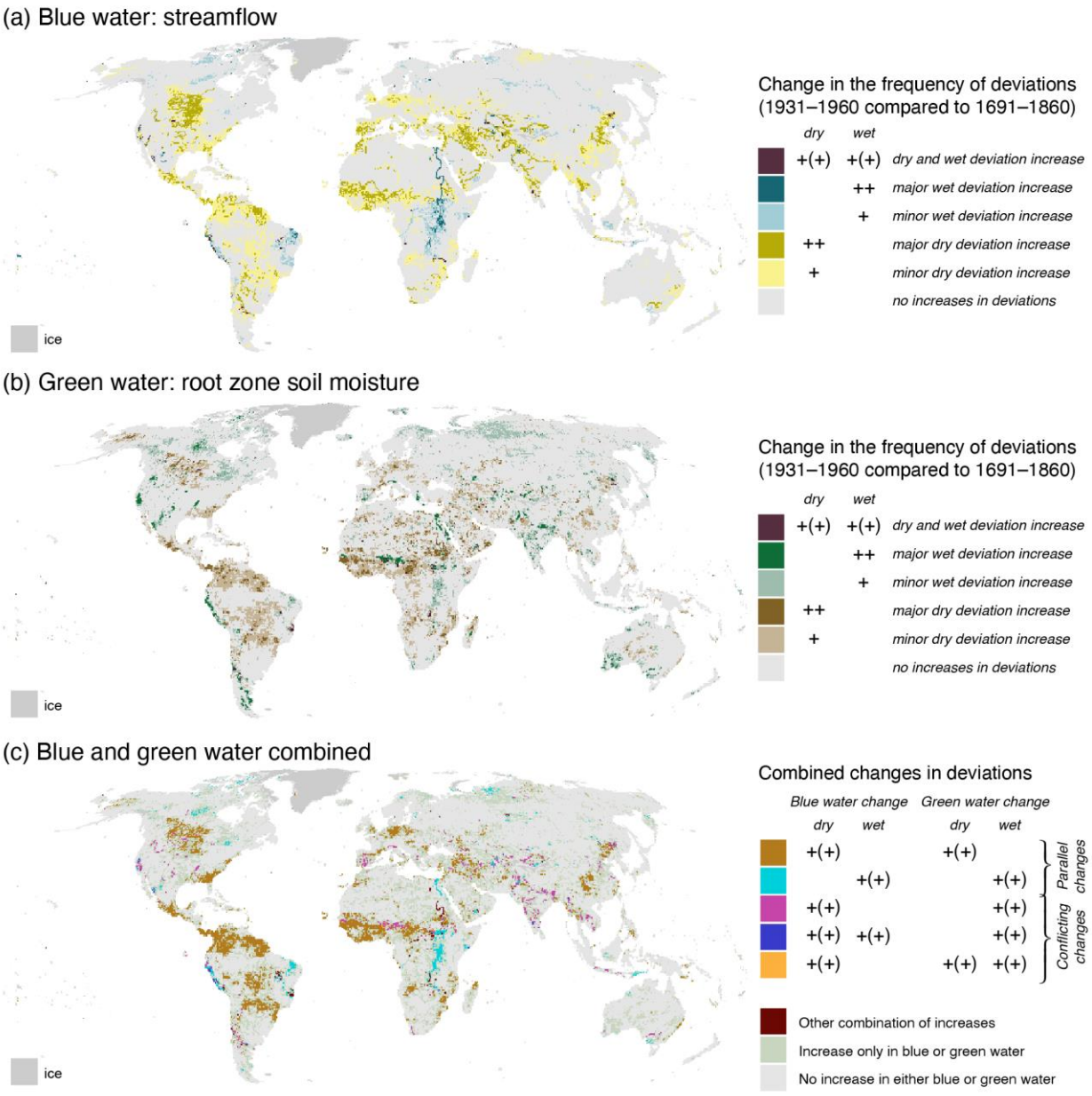

Fig. S9.

Statistically significant increases in local (cell-wise) dry and wet deviations for blue water (a), for green water (b), and for combined blue and green water (c). The changes are computed by comparing the ensemble median frequency of local deviations during 1931–1960 against 1691–1860, and significance of change (p = 0.05) is tested with R package stats function prop.test (*38*). Colors denoted with + indicate statistically significant increases with magnitude less than 5 pp (minor), whereas colors denoted with ++ indicate statistically significant increases with magnitude greater than 5 pp (major). Colors denoted with +(+) pool together any statistically significant increase (minor or major). The combination classes (c) always consist of both blue and green water changes; changes in only one or neither are colored in lighter colors.

simulation period	climate scenario	socio-economic conditions	ISIMIP output variable	GHM	GCMs
pre-industrial	picontrol	1860soc	rootmoist	CLM50	GFDL-ESM2M, HadGEM2-ES, IPSL-CM5A-LR, MIROC5
pre-industrial	picontrol	1860soc	rootmoist	LPJmL	GFDL-ESM2M, HadGEM2-ES, IPSL-CM5A-LR, MIROC5
pre-industrial	picontrol	1860soc	rootmoist	MPI-HM	GFDL-ESM2M, IPSL-CM5A-LR, MIROC5
pre-industrial	picontrol	1860soc	rootmoist	PCR-GLOBWB	GFDL-ESM2M, HadGEM2-ES, IPSL-CM5A-LR, MIROC5
pre-industrial	picontrol	1860soc	dis	H08	GFDL-ESM2M, HadGEM2-ES, IPSL-CM5A-LR, MIROC5
pre-industrial	picontrol	1860soc	dis	LPJmL	GFDL-ESM2M, HadGEM2-ES, IPSL-CM5A-LR, MIROC5
pre-industrial	picontrol	1860soc	dis	MATSIRO	GFDL-ESM2M, IPSL-CM5A-LR, MIROC5
pre-industrial	picontrol	1860soc	dis	MPI-HM	GFDL-ESM2M, IPSL-CM5A-LR, MIROC5
pre-industrial	picontrol	1860soc	dis	PCR-GLOBWB	GFDL-ESM2M, HadGEM2-ES, IPSL-CM5A-LR, MIROC5
pre-industrial	picontrol	1860soc	dis	WaterGAP2	GFDL-ESM2M, HadGEM2-ES, IPSL-CM5A-LR, MIROC5
historical	historical	histsoc	rootmoist	CLM50	GFDL-ESM2M, HadGEM2-ES, IPSL-CM5A-LR, MIROC5
historical	historical	histsoc	rootmoist	LPJmL	GFDL-ESM2M, HadGEM2-ES, IPSL-CM5A-LR, MIROC5
historical	historical	histsoc	rootmoist	MPI-HM	GFDL-ESM2M, IPSL-CM5A-LR, MIROC5
historical	historical	histsoc	rootmoist	PCR-GLOBWB	GFDL-ESM2M, HadGEM2-ES, IPSL-CM5A-LR, MIROC5
historical	historical	histsoc	dis	H08	GFDL-ESM2M, HadGEM2-ES, IPSL-CM5A-LR, MIROC5
historical	historical	histsoc	dis	LPJmL	GFDL-ESM2M, HadGEM2-ES, IPSL-CM5A-LR, MIROC5
historical	historical	histsoc	dis	MATSIRO	GFDL-ESM2M, IPSL-CM5A-LR, MIROC5
historical	historical	histsoc	dis	MPI-HM	GFDL-ESM2M, IPSL-CM5A-LR, MIROC5
historical	historical	histsoc	dis	PCR-GLOBWB	GFDL-ESM2M, HadGEM2-ES, IPSL-CM5A-LR, MIROC5
historical	historical	histsoc	dis	WaterGAP2	GFDL-ESM2M, HadGEM2-ES, IPSL-CM5A-LR, MIROC5

Table S1.

Data sets used in this study, adopting ISIMIP 2b nomenclature (*39*). The *pre-industrial* simulation period represents 200 years of pre-industrial conditions, nominally covering years 1661–1860, and the *historical* simulation period covers years 1861–2005. The climate scenario *picontrol* uses pre-industrial climate and 286 ppm CO2 concentration, while the *historical* climate scenario uses historical climate and CO2 concentration. Socio-economic conditions for the scenario *1860soc* are fixed at the pre-industrial level, while the *histsoc* scenario uses varying historical land use and socio-economic conditions. The ISIMIP output variables *rootmoist* and *dis* refer to root-zone soil moisture (soil moisture) and discharge (streamflow), respectively.